Physical modeling of tsunamis generated by three-dimensional deformable granular landslides

Fahad Mohammed[1,2] and Hermann M. Fritz[2]

Received 21 December 2011; revised 19 September 2012; accepted 21 September 2012; published 15 November 2012.

[1] Tsunamis generated by deformable granular landslides are physically modeled in a three-dimensional tsunami wave basin based on the generalized Froude similarity. The dynamic landslide impact characteristics were controlled by means of a novel pneumatic landslide generator. The wave amplitudes, periods, and wavelengths are related to the landslide parameters at impact with the landslide Froude number being a dominant parameter. Between 1 and 15% of the landslide kinetic energy at impact is converted into the wave train energy. The wave amplitudes decay in radial and angular directions from the landslide axis. The first wave crest mostly travels with speeds close to the theoretical approximation of the solitary wave speed. The measured tsunami wave profiles were either of the nonlinear oscillatory or nonlinear transition type depending primarily on the landslide Froude number and relative slide thickness at impact. The generated waves range from shallow to deep water depth regimes, with the majority being in the intermediate water depth regime. Wave characteristics are compared with other two- and three-dimensional landslide tsunami studies and the results are discussed.

Citation: Mohammed, F., and H. M. Fritz (2012), Physical modeling of tsunamis generated by three-dimensional deformable granular landslides, *J. Geophys. Res.*, *117*, C11015, doi:10.1029/2011JC007850.

1. Introduction

[2] Tsunamis are water waves generated by impulsive disturbances such as submarine earthquakes and landslides, volcanic eruptions and asteroid impacts. Landslides may generate tsunamis in confined water bodies, at islands and continental shelve breaks. Near coastal landslide sources, tsunami waves propagate both in offshore and along the shore directions. Tsunamis generated by landslides are characterized by locally high amplitudes and runup relative to the overall runup distribution, which can be particularly devastative in near field regions and confined water bodies [*Okal and Synolakis*, 2004]. Landslide tsunami events may be categorized as subaerial, partially submerged or submarine landslide-generated tsunamis depending on the initial position of the landslide. Subaerial landslide impact-generated tsunamis with extreme runup heights were recorded at Tafjord (1934) and Lake Loen (1936) in Norway [*Jørstad*, 1968; *Harbitz et al.*, 1993], Lituya Bay, Alaska, in 1958 [*Fritz et al.*, 2001, 2009; *Weiss et al.*, 2009], Vajont dam in Italy in 1963 [*Müller*, 1964], Puerto Aysen, Chile, in 2007 [*Sepúlveda and Serey*, 2009; *Naranjo et al.*, 2009]. A local tsunami was generated by a coastal landslide triggered by the 2010 Haiti earthquake [*Fritz et al.*, 2012]. Major tsunamis caused by submarine landslides were associated with the ancient Storegga slides [*Bondevik et al.*, 2005] and observed at Grand Banks, Newfoundland, in 1929 [*Fine et al.*, 2005] as well as in Papua New Guinea, 1998 [*Synolakis et al.*, 2002; *Bardet et al.*, 2003]. Landslide-generated tsunamis may be caused by volcanic edifice collapses such as at Unzen, 1792 [*Ogawa*, 1924; *Slingerland and Voight*, 1979], Ritter island, 1888 [*Ward and Day*, 2003], and Stromboli, 2002 [*Tinti et al.*, 2005, 2006]. The resulting tsunami events can cause damage because of large runup along the coastline and overtopping of dams. Field data from historic events is commonly limited to landslide scarps, submarine landslide deposits where mapped, trimlines from wave runup and far field tide gauge recordings. Hence landslide-generated tsunamis are physically modeled to study the wave generation process and the near field wave characteristics in a three dimensional physical model.

[3] Two dimensional tsunami generation by granular landslides were studied by *Huber* [1980], *Fritz* [2002], *Fritz et al.* [2003a, 2003b, 2004, 2009], *Zweifel and Hager* [2006] and *Heller and Hager* [2010]. Some of the two- and three-dimensional experiments by *Huber* [1980] were analyzed by *Huber and Hager* [1997]. Previously, two dimensional landslide tsunami experiments were extensively performed in flumes with a solid block sliding down an incline [*Russell*, 1837, 1844; *Wiegel*, 1955; *Law and Brebner*, 1968; *Wiegel et al.*, 1970; *Kamphuis and Bowering*, 1970; *Slingerland and Voight*, 1979; *Heinrich*, 1992; *Watts*, 1997, 1998, 2000; *Walder et al.*, 2003; *Grilli and Watts*, 2005; *Sælevik*, 2009; *Sælevik et al.*, 2009]. Block models do not reproduce the long

[1]School of Civil and Environmental Engineering, Cornell University, Ithaca, New York, USA.
[2]School of Civil and Environmental Engineering, Georgia Institute of Technology, Savannah, Georgia, USA.

Corresponding author: F. Mohammed, School of Civil and Environmental Engineering, Cornell University, 220 Hollister Hall, Ithaca, NY 14853, USA. (fm353@cornell.edu)

0148-0227/12/2011JC007850

subaqueous landslide runout observed in nature [*Hampton et al.*, 1996]. Piston wave makers were proposed to further study landslide-generated tsunami waves [*Miller*, 1970; *Hammack*, 1973; *Sander and Hutter*, 1992; *Sœlevik et al.*, 2009]. This may apply to rare cases with landslide thickness exceeding water depth such as Vajont reservoir [*Müller*, 1964, 1968] and Sprit Lake at Mount St. Helens [*Voight et al.*, 1981, 1983]. Forced piston motion and the fixed shape were the main disadvantages in those studies. *Sœlevik et al.* [2009] concluded in a limited comparison with *Fritz et al.* [2004] that solid and granular slides result in different cavity collapse regimes. The difference in block and granular slide models may be attributed to the difference in porosity, slide front angle, blockage ratio, transition at slope toe and slide rigidity [*Heller and Kinnear*, 2010]. Waves generated by three dimensional solid block landslides were studied by *Liu et al.* [2005], *Panizzo et al.* [2005], *Enet and Grilli* [2005, 2007], *Ataie-Ashtiani and Najafi-Jilani* [2008], *Ataie-Ashtiani and Nik-Khah* [2008] and *Di Risio et al.* [2009] on flat bottoms, on sloping beaches and conical islands. The present study focused on the three-dimensional subaerial and subaqueous granular landslide motion, tsunami wave generation and propagation and the lateral onshore runup.

2. Physical Model

[4] The three-dimensional experiments on tsunami generation by landslides were conducted in the tsunami wave basin (TWB) of the Network for Earthquake Engineering Simulation (NEES) at Oregon State University in Corvallis, Oregon, USA. Tsunamis were generated in the wave basin measuring 48.8 m in length, 26.5 m in width, with varying still water depths h = 0.3, 0.6, 0.9 and 1.2 m. A hillslope inclined at $\alpha = 27.1^\circ$ with a smooth 9.3 m long steel plate as a sliding surface was constructed on the west end of the basin. Landslides were modeled with naturally rounded river gravel with the following parameters: particle size range from 6.35 to 19.05 mm, d_{50} = 13.7 mm, ρ_g = 2.6 t/m^3, landslide bulk density ρ_s = 1.76 t/m^3, porosity n_{por} = 0.31, effective internal friction angle $\phi' = 41^\circ$ and dynamic bed friction angle $\delta = 23^\circ$ on the sliding surface. The slip between the bed and the granular mass was dominant resulting in slug-type flow [*Savage and Hutter*, 1989]. The granular material used in the experiment scales to rock type subaerial landslides in the field and the bulk characteristics are comparable to the granular materials used in earlier studies [*Huber*, 1980; *Fritz et al.*, 2004]. The rheology of the material used is limited to granular sliding rheology or rate-dependent rheology, which translates to basal sliding or collisional effects [*Savage*, 1979]. The scaling in the present experimental results may not be applicable to cohesive materials such as clay and potential effects of small-scale granular particles such as sand and silt [*Iverson et al.*, 2004; *Rickenmann*, 1999; *Schatzmann et al.*, 2003]. The landslide characteristics at impact were controlled by means of a novel pneumatic landslide tsunami generator [*Fritz et al.*, 2009]. The landslide was characterized by the landslide volume V_s, slide front velocity v_s, landslide length l_s, thickness s and width b on the hillslope at impact. The intersection of the hillslope with the shoreline marks the location of the landslide impact, which varies with the water depth in the TWB. The water body and wave parameters are the still water depth h, distance from impact r, direction relative to landslide propagation θ, water surface elevation $\eta(r, \theta, t)$, wave height H, wave amplitude a, wave period T, wavelength λ and wave speed c. The crest and trough amplitudes are denoted by the subscripts a_c or a_t. Based on scaling analysis, the subaerial landslide shape and motion are described by dominant nondimensional parameters: landslide Froude number, $F = v_s/\sqrt{gh}$, relative landslide thickness $S = s/h$, relative width $B = b/h$ and relative volume $V = V_s/h^3$. The unconfined deformable nature and long runout lengths of granular landslides complicates length measurements because of the characteristic bulk front followed by an asymptotically thinning tail. Hence a length scale for the granular landslide L_s is defined as $L_s = V_s/(sb)$, which leads to a relative slide length $L = L_s/h$. The wave propagation in the basin is in the range $0 \le R \le 80$ and $0 \le \theta \le 90^\circ$, where $R = r/h$ is the propagation distance relative to the water. Two initial landslide lengths were emplaced in the slide box of the landslide tsunami generator while maintaining constant initial thickness and width, thereby varying the landslide volume for wave generation [*Mohammed and Fritz*, 2010]. The relative volume is strongly varied by altering the water depth in the denominator of the expression $V = V_s/h^3$. This resulted in nondimensional landslide parameters in the following ranges: landslide Froude number at impact, $1 < F < 4$, relative landslide thickness, $0.1 < S < 0.9$, relative landslide width, $1 < B < 7$, relative landslide length, $2.5 < L < 6.8$ and relative landslide volume, $0.25 < V < 30$. The data from 64 trials in the experiments of 2006 [*Mohammed*, 2010] and 24 trials from 2010 [*Mohammed et al.*, 2011] are combined and presented below to study wave generation and basin wide wave propagation.

3. Instrumentation Setup

[5] The landslide velocity prior to release from the slide box is measured using the string pot data. Several above and three under water cameras recorded the landslide shape and kinematics along the hillslope and in the tsunami wave basin. The particle image velocimetry (PIV) analysis of selected high-resolution image sequences resulted in subaerial landslide surface velocity vector maps [*Fritz et al.*, 2009]. The general setup of the instrumentation in the wave basin is shown in Figure 1a. A total of 25 wave gauges were installed in the tsunami wave basin to measure the water surface profiles. Twenty one wave gauges recorded the basin wide wave propagation in radial and angular direction away from the landslide source, while four slope parallel gauges in combination with overhead cameras recorded the lateral wave propagation and wave runup along the hillslope. The wave gauge configuration in the tsunami wave basin at water depth of h = 0.6 m is shown in Figure 1b. The wave gauges are of resistance type, where the conductivity of the water medium is used to determine the wave height [*Hughes*, 1993]. Two wave gauge designs were deployed consisting of cantilevered parallel twin 3.2 mm diameter stainless steel rods and suspended twin stainless wires, respectively. The calibration of the wave gauges highlights the linearity over the 0.5 m range with a maximum error of 0.7%. The largest wave gauge error source is attributed to potential variations in water resistivity over time on the order of 2%. The wave gauge calibration factors were determined during the filling

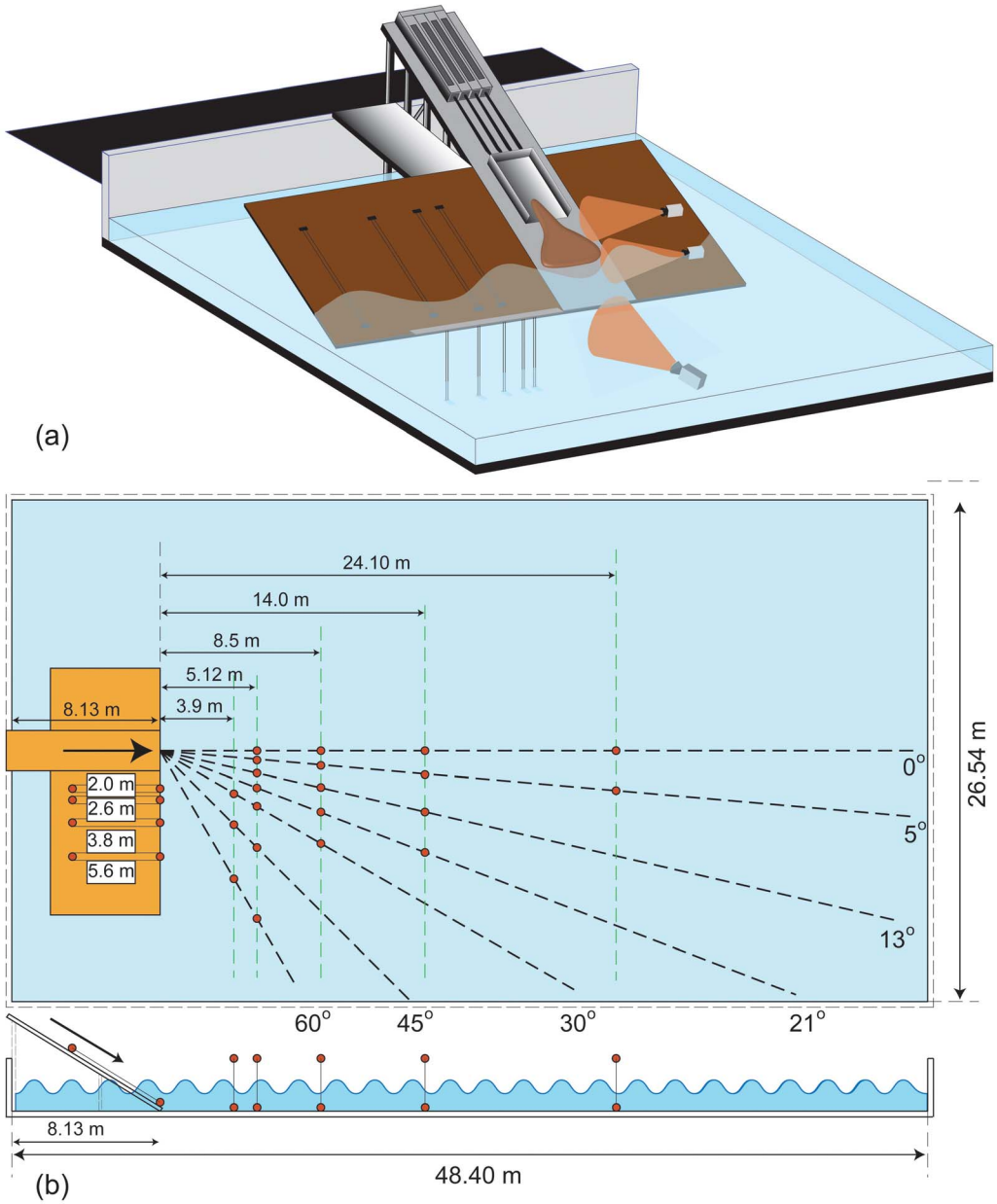

Figure 1. (a) The pneumatic landslide tsunami generator on the hillslope in the Network for Earthquake Engineering Simulation (NEES) tsunami wave basin at the O.H. Hinsdale wave research laboratory at Oregon State University, Corvallis. (b) The wave gauge array used to measure the water surface elevation of the tsunami wavefronts generated by the three-dimensional deformable granular landslides.

of the tsunami wave basin by relating the analog voltage output signals to the corresponding water depths measured with an acoustic water level.

4. Landslide Source Characteristics

[6] The subaerial landslide motion is measured from the combined recordings of the four cable extender transducers, the above water side-view video and high-resolution overhead cameras. The time history of the landslide front is obtained to measure the velocity of the slide motion up to the moment of impact. Initially the slide is contained and accelerated in the box (2.1 m × 1.2 m × 0.3 m), with the slide velocity corresponding to the box velocity. The landslide is released as the box reaches the maximum velocity. The deformable granular landslide collapses down the hillslope while the box is decelerated and flows down simulating a gravity driven inertial granular landslide (Figure 2a). Across the bulk of the landslide width, the velocity is mostly uniform. The velocity diminishes with decreasing thickness toward the edge of the slide [*Mohammed*, 2010]. The front velocity at impact is in the range $2.2 < \frac{v_s}{\sqrt{gs_0}} < 3.8$ for the

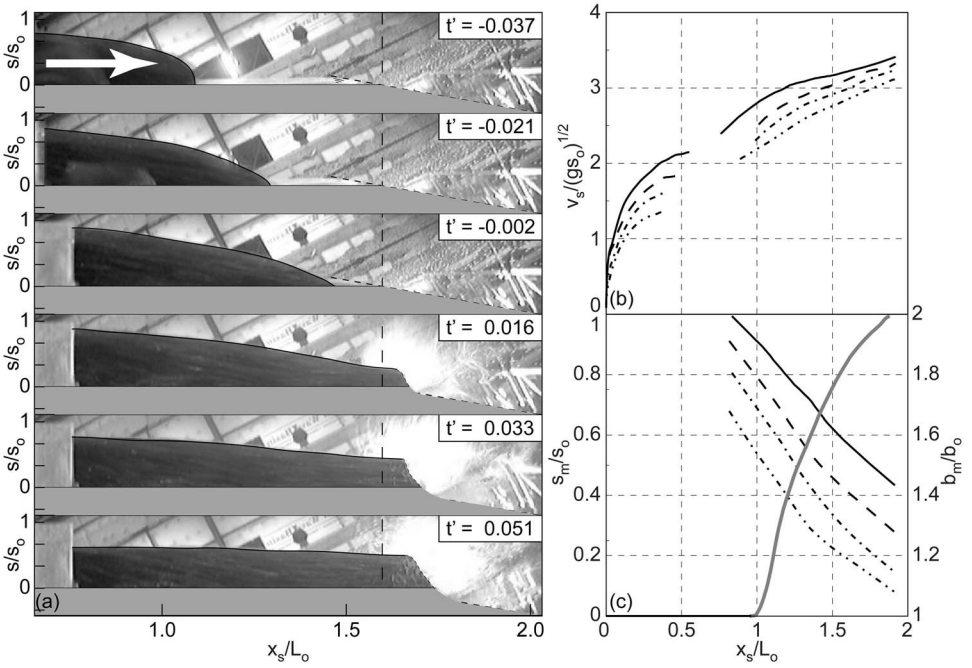

Figure 2. Subaerial deformable granular landslide on an $\alpha = 27.1°$ hillslope: (a) image sequence from an above water side camera showing the slide profile, front evolution and impact with water surface. Nondimensional time $t' = \sqrt{g/s_0}$, with initial slide thickness $s_0 = 0.3$ m, slide impact on the water surface $t' = 0$, propagation distance x_s, and initial slide length $L_0 = 2.1$ m; (b) slide front velocity measured by a combination of string extender transducers $\left(x_s/L_0 < 0.7\right)$ on the slide box and above water camera image sequences $\left(x_s/L_0 > 0.7\right)$; (c) maximum slide thickness and width (solid gray line) (normalized by initial width ($b_0 = 1.2$ m) measured by the above water cameras on the hillslope. Initial location of the slide front $x_s = 0$ and slide launch velocities of $v_s/\sqrt{gs_0} = 1.3$ (dash dot dot line), 1.6 (dash dot line), 1.8 (dashed line), and 2.2 (solid line).

landslide volumes of $V_s = 0.756$ m^3 and 0.378 m^3, where s_o is the initial slide thickness and g is the gravitational acceleration. The evolution of the landslide front velocity along the downslope propagation distance is shown in Figure 2b. Similar measurements are made for the slide thickness and width along the hillslope up to the impact. The landslide thickness at impact was in the range $0.1 < \frac{s}{s_0} < 0.6$. The

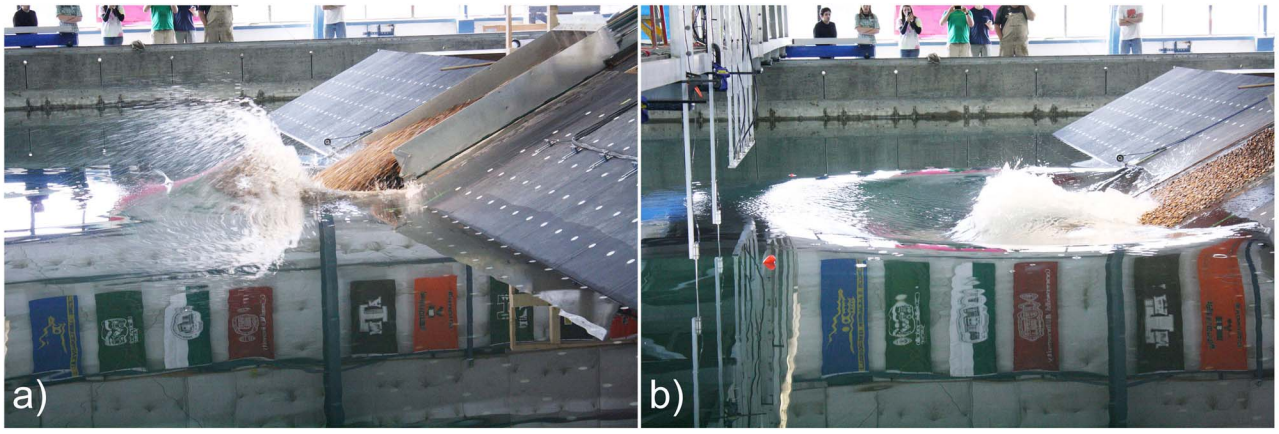

Figure 3. (a) Granular landslide impact with the water body showing water displacement and impact crater formation at $h = 1.2$ m. (b) The leading wave crest followed by the trough is shown (Photo credit: Devin K. Daniel, NEES REU 2010).

maximum landslide thickness and width along the downslope propagation distance from the release to the water line at various water depths is shown in Figure 2c. The location of landslide impact along the hillslope is given by the water depth and allows to determine the key slide impact parameters.

5. Tsunami Wave Generation

[7] Landslides generate tsunami waves by a rapid or an impulsive transfer of momentum from the landslide mass to the water body during the impact and subaqueous runout. The impact and penetration of the landslide into the water body results in an initial wave crest. The displaced water moves primarily in the direction of the landslide and laterally around the landslide front (Figure 3). The initial water displacement develops into a radial wavefront. When the drawdown reaches the maximum, the restoring gravitational forces drive the water surface rebound. The runup and rundown on the hillslope form the second wave amplitudes of the radial wavefront. Subsequent oscillations with attenuating runup and rundown of the water surface at the shoreline forms the trailing wave train. Transverse displacement of water results in the lateral edge waves on the hillslope, which coincide with the corresponding radial wavefront. The leading lateral waves and the leading wavefront form the first radial wavefront which is generated by the landslide impact. The runup and draw down oscillations are driven by a combination of the landslide motion after the initial impact and the dynamic variations of the water surface elevation in the impact region. The scale of water surface depression varies with the slide impact velocity and thickness. This variation occurs since the impact velocity along with the slide cross-section area determines the rate of mass and momentum flux at impact. An image sequence of the wave generation by landslide impact is shown in Figure 4.

6. Wave Propagation

6.1. Wave Profiles

[8] Landslide-generated tsunami waves were classified into weakly nonlinear oscillatory, nonlinear transition, solitary like and dissipative transient bores based on 2-D block slide experiments by *Noda* [1970] and 2-D granular landslide experiments by *Fritz et al.* [2004]. These classifications depend on the landslide Froude number F and thickness S at impact. The lower limit of slow and thin landslides generate nonlinear oscillatory waves while fast and thick landslides can lead to dissipative transient bores. In the present three-dimensional study, nonlinear oscillatory and nonlinear transition type of waves were observed. The classification was based on the wave profile measurements and analysis of the wave train beyond the first three waves. Solitary and bore-type tsunami waves were not observed in the present 3-D study beyond the immediate impact and splash zone. The nonlinear oscillatory waves are characterized by a leading main wave crest followed by a dispersive oscillatory wave train, while the nonlinear transition waves have a main leading wave crest and trough followed by a weakly dispersive wave train. A recorded wave profile representing the nonlinear oscillatory wave type and the corresponding energy spectrum in the time-frequency domain are shown in Figure 5a for a slide impact at $F = 1.87$, $S = 0.12$, $V = 1.75$, and $h = 0.6$ m. The corresponding basin wide tsunami propagation is shown in Figure 6. Wavelet transforms of the wave profiles are used to identify the energy distribution in the

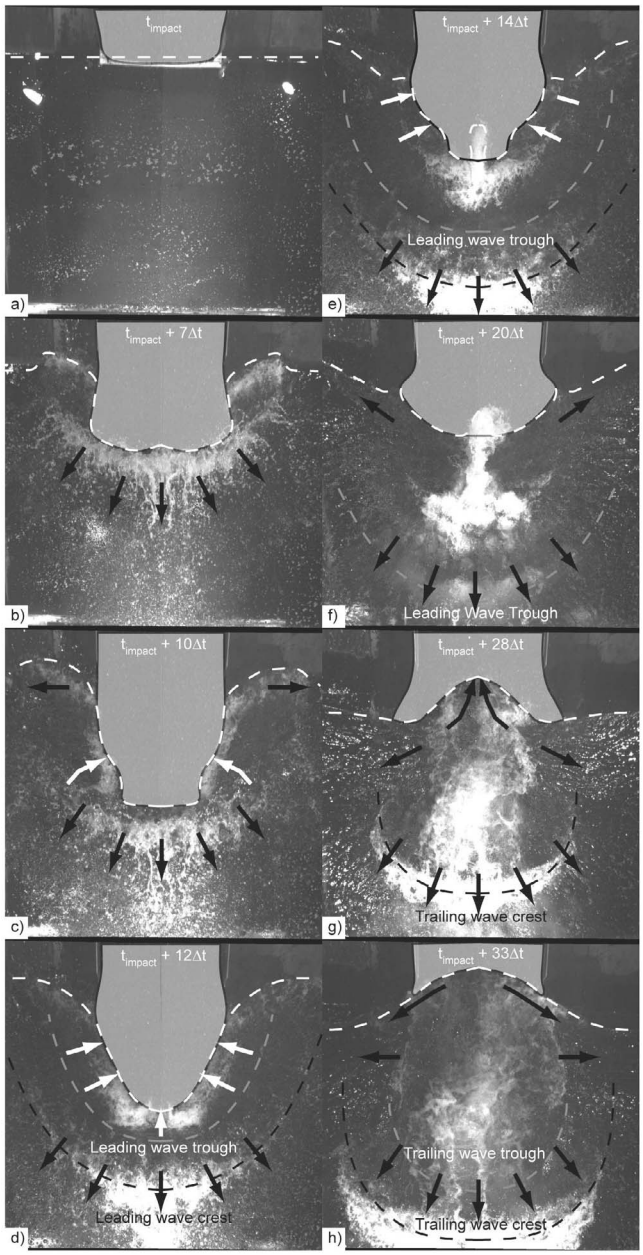

Figure 4. Tsunami wave generation by three-dimensional deformable granular landslides shown for landslide Froude number $F = 1.4$, relative slide thickness $S = 0.23$, relative slide volume $V = 0.44$ at water depth $h = 1.2$ m. (a) Time of initial impact of landslide front with water surface, (b, c) water displacement by the impact and surface depression, (d) initiation of surface restoration, (e) surface restoration and radial wave propagation, (f) surface collapse and generation of first trailing wave, (g) wave runup on the hillslope post collapse, and (h) end of collapse of surface depression. Selected image sequence from a video recording at 15 frames per second.

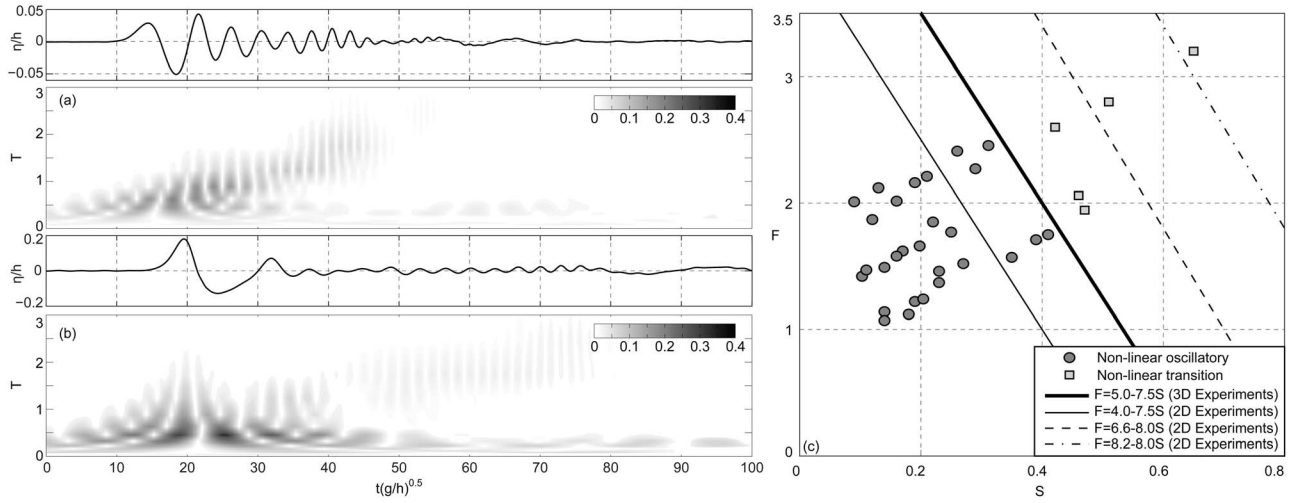

Figure 5. Observed wave types: (a) nonlinear oscillatory wave profiles and wavelet energy spectrum shown in time-frequency domain for $F = 1.87$, $S = 0.12$, $V = 1.75$, $h = 0.6$; (b) nonlinear transition type of waves and corresponding energy spectrum at $F = 3.1$, $S = 0.75$, $V = 28$, $h = 0.3$ m; and (c) observed nonlinear oscillatory and nonlinear transition type of waves in the present three-dimensional study compared with transition lines between nonlinear oscillatory, nonlinear transition and solitary-type waves observed in two-dimensional granular landslide experiments [*Fritz et al.*, 2004].

wave and the wave grouping in the time-frequency domain [*Liu*, 2000; *Panizzo et al.*, 2002]. These waves are characterized by a strong frequency dispersion, which stretches the wave train and transiently enhances trailing waves during propagation. While the initial impact generates the leading waves, the trailing waves are generated by a superposition of wave generation by slow flux of tailward thinning landslide material into the water body and attenuating periodic oscillations of the shoreline in the impact region. The nonlinear oscillatory wave type is observed for relatively slower and thinner landslides in the present study.

[9] The nonlinear transition wave type is characterized by a long trough separating the leading wave crest and the weakly dispersive trailing wave. A recorded wave profile representing the nonlinear transition wave type and the corresponding wavelet energy spectrum in the time-frequency domain are shown in Figure 5b for a slide impact at $F = 3.1$, $S = 0.75$, $V = 28$, and $h = 0.3$ m. The corresponding basin wide tsunami propagation is shown in Figure 7. This wave type is observed for relatively faster and thicker landslides in the present study. While the initial impact generates the leading waves, the weakly dispersive trailing waves are generated primarily by attenuating shoreline oscillations in the impact region.

[10] All observed tsunami wave trains stretch apart with the propagation distance because of dispersion and nonlinearity. The leading waves decay with propagation distance while dispersion temporarily enhances subsequent trailing waves [*Løvholt et al.*, 2008]. Hence, far away from the source region, the trailing waves may be more destructive than the leading tsunami wave [*Ward*, 2001; *Fritz and Borrero*, 2006]. In the present study, the observed nonlinear oscillatory and transition wave-type regimes are shown in Figure 5c. The transition from the nonlinear oscillatory to the nonlinear transition wave-type regime is shifted toward relatively higher values of the nondimensional parameters F and S ($F = 5 - 7.5\,S$) in comparison with two-dimensional granular landslide studies by *Fritz et al.* [2004] ($F = 4 - 7.5\,S$).The nonlinear oscillatory wave type is observed for relatively slow and thin landslides at impact. Relatively faster and thicker landslides generate the nonlinear transition wave type.

6.2. Wave Amplitudes

[11] Near the landslide source, impulsively generated tsunami waves may be nonlinear with first and second crest and trough amplitudes departing from linear equipartition theory. Since individual components of the wave train travel at different speeds, the wave crests and troughs are considered independently. The wave crest is identified from an upcrossing to a subsequent downcrossing point in the wave train, while the trough is defined from a downcrossing to an upcrossing point. Thus, the wavelength, wave period and wave speed are analogously considered. The surface envelope for the leading wave crest and trough amplitude for a landslide impact with impact Froude number $F = 3$, relative landslide thickness $S = 0.75$, relative width $B = 4.7$ at impact and relative volume $V = 28$ is shown in Figures 8a and 8b. The surface envelope decays in both the radial and angular direction. The relative wave amplitude increases with increasing slide thickness relative to the water depth. The parametric equation for the wave crest and trough can be represented as

$$\frac{a_{c1}}{h} = k_a f\left(\frac{r}{h}, \theta\right) \tag{1}$$

by decoupling the wave generation mechanism through the function k_a and the propagation characteristics through the function f with amplitude a, water depth h, radial propagation

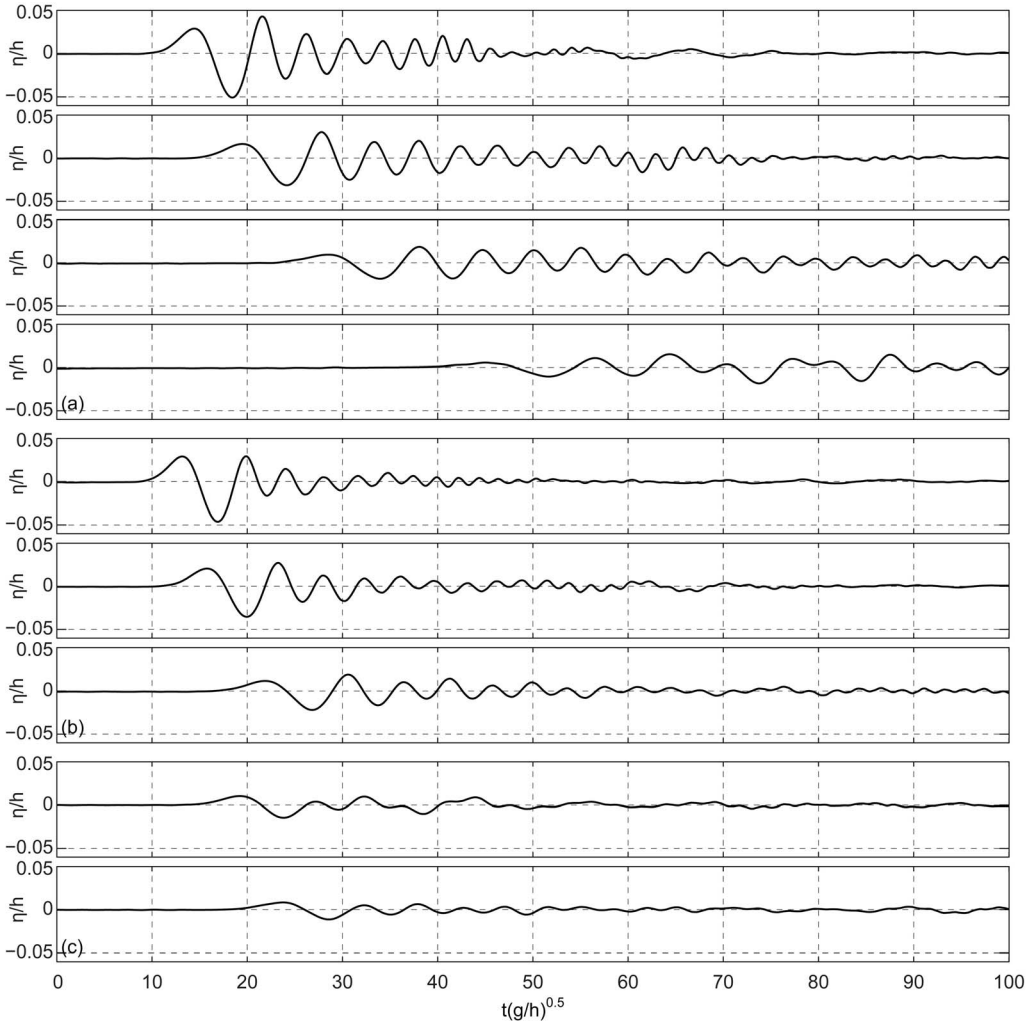

Figure 6. Propagation of nonlinear oscillatory waves at $F = 1.87$, $S = 0.12$, $V = 1.75$, $h = 0.6$ m measured at (a) $\theta = 0°$, $r/h = 9.0, 14.2, 23.3, 40.2$, (b) $\theta = 30°$, $r/h = 7.7, 10.3, 16.4$, and (c) $\theta = 60°$, $r/h = 13.3, 17.3$.

distance r and angular direction θ with reference to the direction of the landslide prolongation. Multi variable regression analysis lead to the empirical equations for the individual wave amplitudes as

$$\frac{a_{c1}}{h} = k_{ac1}\left(\frac{r}{h}\right)^{n_{ac1}} \cos\,\theta \tag{2a}$$

$$\frac{a_{t1}}{h} = k_{at1}\left(\frac{r}{h}\right)^{n_{at1}} \cos\,\theta \tag{2b}$$

$$\frac{a_{c2}}{h} = k_{ac2}\left(\frac{r}{h}\right)^{n_{ac2}} \cos^2\,\theta \tag{2c}$$

for the first wave crest and trough and second wave crest, respectively. The second wave crest amplitude decays faster in the angular direction compared with the leading wave amplitude. The variation in the decay rate is due to differences in the wave generation mechanism between the leading and trailing waves. The direct impact of the bulk landslide mass generates the first wave, while the uprush following the water surface depression generates the trailing wavefront. The attenuations of the first wave crest and trough amplitudes are shown in Figure 9 normalized by the angular decay and the wave generation functions. The decay rate n_a of the wave amplitudes with the radial propagation distance represents radial spreading of the wave, amplitude decay due to frequency dispersion and nonlinear effects. The radial decay of the wave amplitudes depends on the landslide characteristics at impact. The trailing wave amplitude evolutions were nonuniform. In some cases, the amplitudes were found to decay initially only to temporarily increase again because of dispersion effects.

[12] The wave generation depends on the landslide characteristics and is expressed as $k_a = f(S, B, L, F, \alpha)$. Multi variable regression analysis combined with insight on the wave generation process provide the empirical equations to

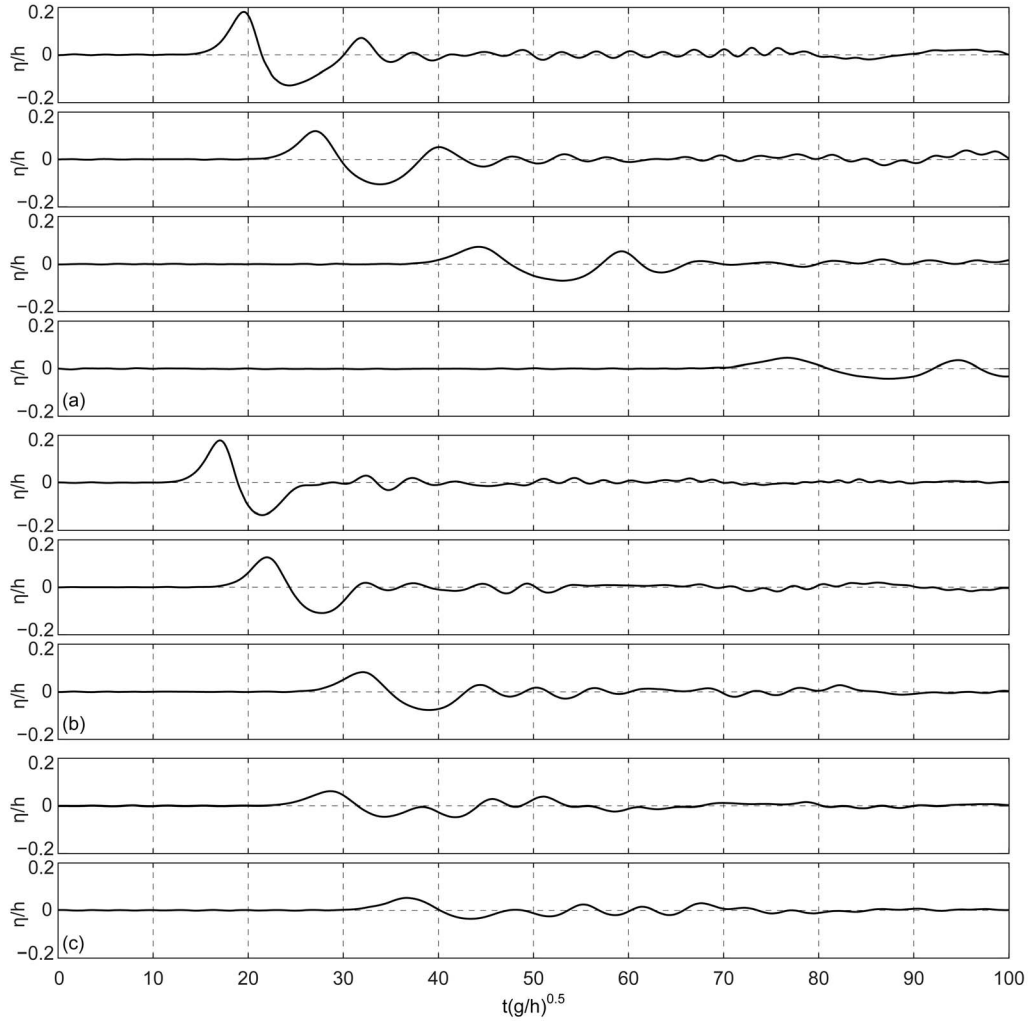

Figure 7. Propagation of nonlinear transition waves at $F = 3.1$, $S = 0.75$, $V = 28$, $h = 0.3$ m measured at (a) $\theta = 0°$, $r/h = 18.0, 28.4, 46.6, 80.4$, (b) $\theta = 30°$, $r/h = 14.14, 20.6, 32.8$, and (c) $\theta = 60°$, $r/h = 26.6, 34.6$.

predict the wave amplitudes and associated decay rate. The resulting wave generation functions and radial decay rates are

$$k_{ac1} = 0.31F^{2.1}S^{0.6} \tag{3a}$$

$$k_{at1} = 0.7F^{0.96}S^{0.43}L^{-0.5} \tag{3b}$$

$$k_{ac2} = 1.0FS^{0.8}B^{-0.4}L^{-0.5} \tag{3c}$$

$$n_{ac1} = -1.2F^{0.25}S^{-0.02}B^{-0.33} \tag{3d}$$

$$n_{at1} = -1.6F^{-0.41}B^{-0.02}L^{-0.14} \tag{3e}$$

$$n_{ac2} = -1.5F^{0.5}B^{-0.07}L^{-0.3} \tag{3f}$$

[13] The comparisons between the measured and predicted values of the first wave crest and trough amplitudes are shown in Figure 10 with correlation coefficients of 0.94 and 0.91, respectively. The maximum deviation of the empirical fit is found to be ±27% for both. The accuracy of the wave amplitude predictions decreases from the front toward the back of the wave train. The leading wave crest amplitude generated by the initial landslide impact is primarily determined by the relative landslide thickness S and slide Froude number F, which were dominant in 2-D granular landslide experiments [*Fritz et al.*, 2004]. The relative landslide width B and length L have limited effects on the leading wave crest amplitude near the source. The radial decay rate depends weakly on the landslide Froude number and inversely on the width at impact. Increased width at impact leads to a more two-dimensional source with less radial decay while decreasing width leads to a one-dimensional point source with increased radial decay. The leading trough is dependent on the relative slide thickness, Froude number and additionally, on the landslide length. Since the trough is generated by the water surface drawdown behind the penetrating

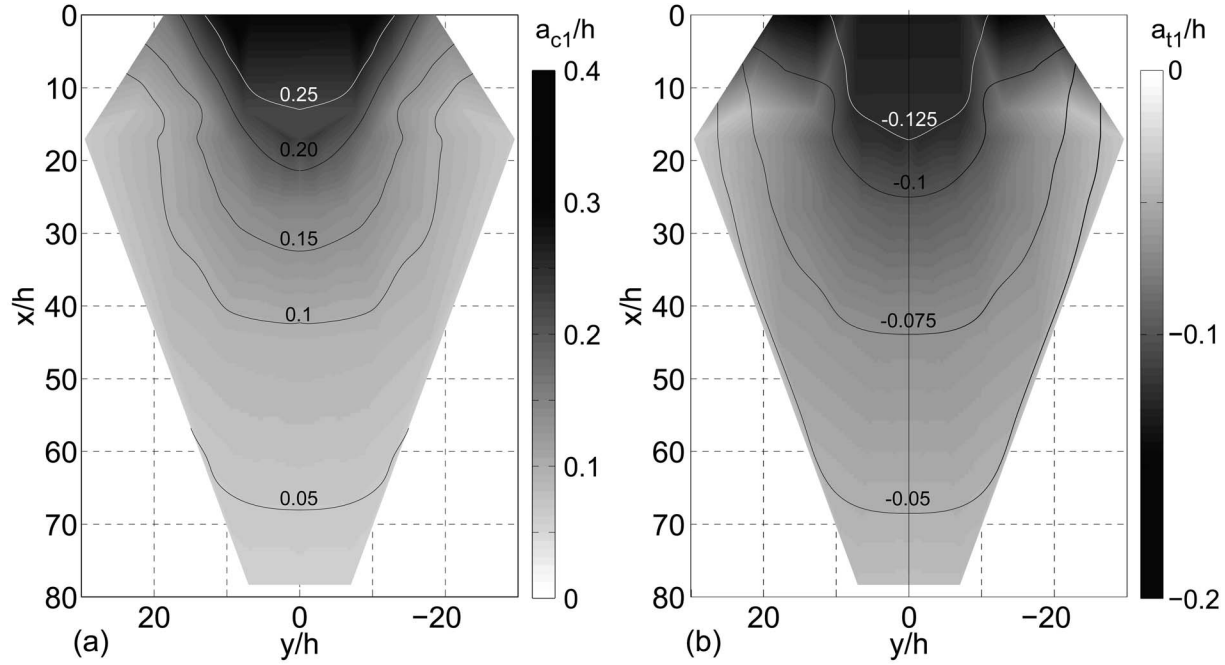

Figure 8. Measured wave surface envelope of (a) first wave crest amplitude a_{c1}/h and (b) first wave trough amplitude a_{t1}/h, shown for $F = 3$, $V = 28$, $S = 0.75$, $B = 4.7$ at $h = 0.3$ m.

landslide, the duration of the depression is dependent on the landslide velocity and length scales. Post impact, the collapse of the impact crater depends on the balance between the flux of the material and the water surface restoring forces. For slower slides, the refilling takes place along with the flux of the slide material, while for faster slides, the refilling is solely dependent on the water surface restoring forces. This leads to the addition of the relative landslide length L in the regression analysis. The trailing waves are generated by the attenuating water surface oscillations following the initial landslide impact, water surface draw down and runup along the hillslope. Since the water surface depression is determined by the nondimensional landslide parameters, the trailing wave amplitudes may be related to the landslide parameters.

[14] Experiments on 3-D wave generation by solid blocks were carried out by *Panizzo et al.* [2005]. The experiments were conducted in a 12 m long, 6 m wide and 0.8 m deep basin. The landslides were modeled as symmetric solid blocks with zero porosity and density $\rho_s = 2200$ kg/m^3, sliding on a rectangular trolley down a ramp. A system of springs at the toe of the ramp inhibits the landslide runout on the flat basin. The still water depths were 0.4 m and 0.8 m with hillslope angles $\alpha = 16°, 26°, 36°$. The generated wave types were classified based on wavelet analysis [*Panizzo et al.*, 2002]. The relative time of underwater landslide motion, t_s^* was found to be a key parameter for describing the generated waves similar to *Watts* [2000].

$$t_s^* = 0.43\left(\frac{bs}{h^2}\right)^{-0.27} F^{-0.66}(\sin\alpha)^{-1.32} \tag{4}$$

[15] The near field maximum and first wave height predicted by *Panizzo et al.* [2005] are given as

$$\frac{H_m}{h} = 0.07\left(\frac{t_s^*}{A_w^*}\right)^{-0.45}(\sin\alpha)^{-0.88}e^{0.6\cos\theta}\left(\frac{r}{h}\right)^{-0.44} \tag{5a}$$

$$\frac{H_1}{h} = 0.07 t_s^{*-0.3} A_w^{*0.88}(\sin\alpha)^{-0.8}e^{1.37\cos\theta}\left(\frac{r}{h}\right)^{-0.81} \tag{5b}$$

where $A_w^* = bs/h^2$ is the nondimensional slide front surface area. The wave height is computed by using the measured landslide parameters at impact. The duration of the underwater landslide runout down the slope and along the horizontal basin floor is unconfined in the 3-D granular landslide experiments. In contrast, a system of mechanical springs at the base of the ramp significantly crops the duration of underwater block landslide motion in the work of *Panizzo et al.* [2005]. Therefore inserting the measured long granular landslide runout durations from this study into the empirical wave height prediction equation by *Panizzo et al.* [2005] results in an underestimation of tsunami heights by a factor of 2 as shown in Figure 11a. Doubling the prediction equation by *Panizzo et al.* [2005] results in a correlation coefficient of 0.94 with this studies experimental data. *Panizzo et al.* [2005] provide a constant radial decay function for the wave height while in this study the observed radial decay rate depends on the landslide source at impact.

[16] *Huber* [1980] conducted outdoor experiments with a rotating flap releasing a two dimensional granular rock avalanche from rest in a 0.5 m wide inclined channel as hillslope

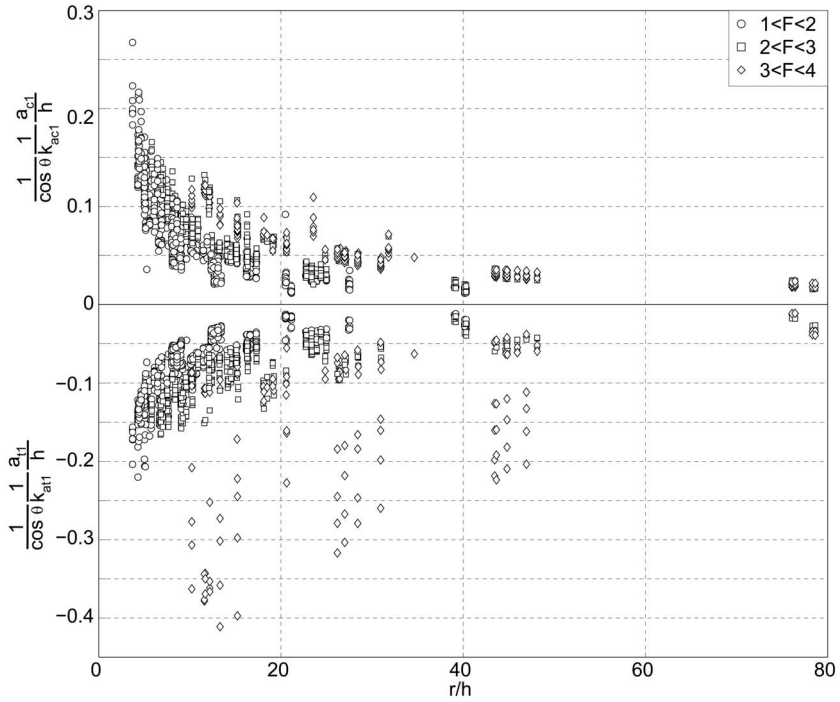

Figure 9. Wave amplitude decay with propagation distance from source, normalized with the angular decay function for first wave crest amplitude a_{c1} and first wave trough amplitude a_{t1}.

or "Sturzbahn" with laterally confining vertical sidewalls. This identical "Sturzbahn" setup with $28^\circ \leq \alpha \leq 60^\circ$ was deployed both in a 0.5 m wide and 30 m long two-dimensional channel and in a 6 m wide and 10 m long basin. In both the 2-D and 3-D experiments the still water depths ranged from 0.12 to 0.36 m. The basin represents approximately a 1:5 horizontal-scale model of the tsunami wave basin (TWB) in this study. *Huber* [1980] deployed the "Sturzbahn" channel at the center of the basin's long side limiting the measurable wave propagation to $\frac{r}{h} \leq 30$. The submerged stretch of the "Sturzbahn" lacked both sidewalls and lateral hillslope extensions resulting in complex hydrodynamics around the submerged 0.5 m wide hillslope. Therefore the lateral runup

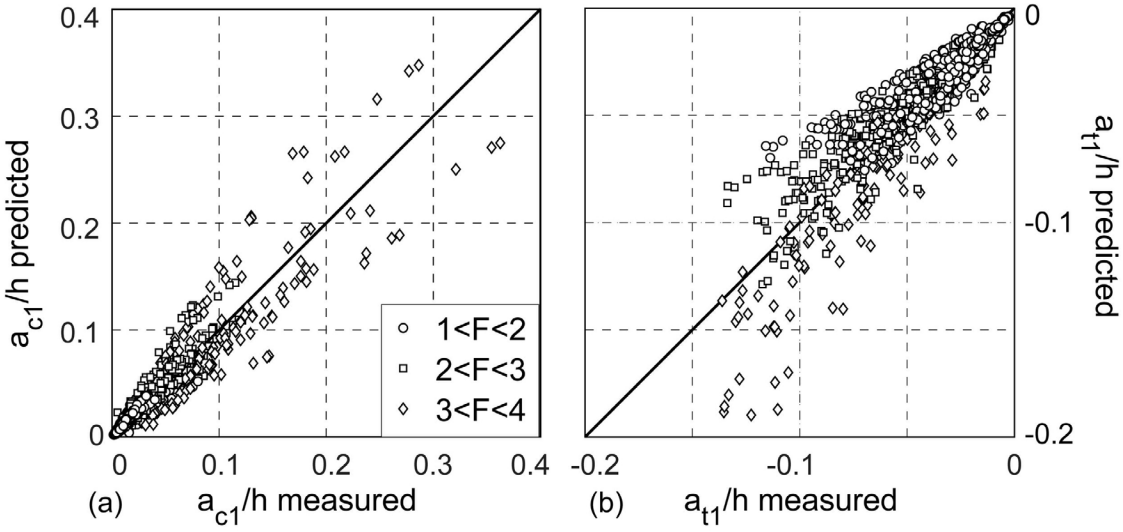

Figure 10. Comparison between measured values and predicted values: (a) first wave crest amplitude, a_{c1}/h, computed with equations (2a) and (3a) and (b) first wave trough amplitude, a_{t1}/h, computed with equations (2b) and (3b).

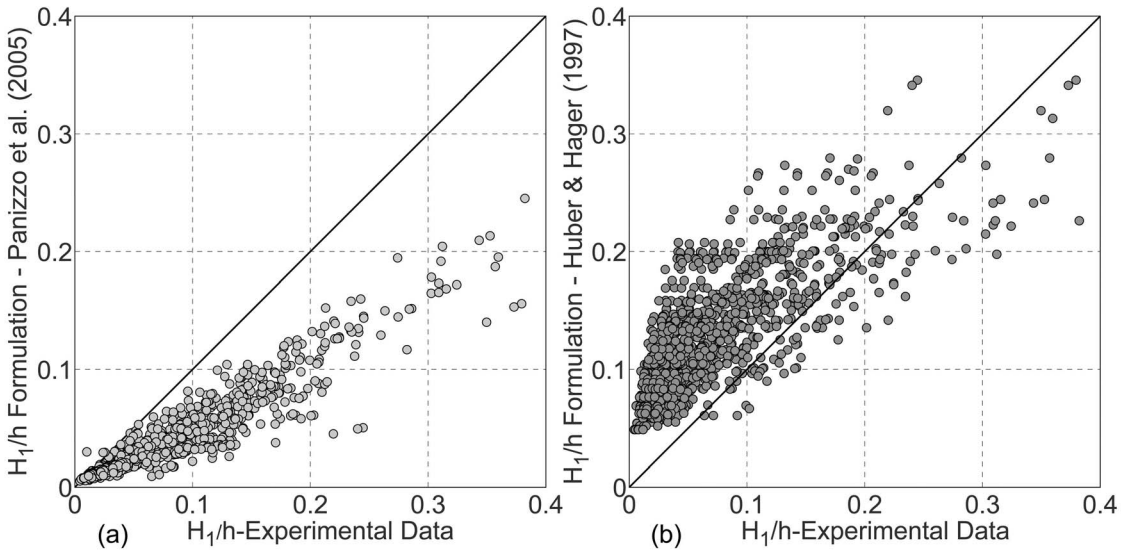

Figure 11. Comparison of measured first wave height H_1/h with predictive equations by (a) *Panizzo et al.* [2005] and (b) *Huber and Hager* [1997].

and edge wave propagation characteristic of coastal settings were absent in the physical model. Landslides were modeled with naturally rounded river gravel with the following parameters: particle size range from 8 to 30 mm, d_{50} = 20 mm, and an internal friction angle $\phi = 32°$. *Savage and Hutter* [1989] reanalyzed the granular flow on the inclined plane and presented two numerical finite difference models. *Huber and Hager* [1997] presented some results of the two and three dimensional experiments conducted by *Huber* [1980], but the derived empirical equations for both the 2-D and 3-D wave height predictions lack correlation coefficients with the experimental data. *Huber and Hager* [1997] plot a radial wave height distribution and decay without showing any underlying experimental data. The predictive 3-D equation for the maximum wave height was obtained as

$$\frac{H_m}{h} = 2 \times 0.88 \sin\alpha \cos^2\left(\frac{2\theta}{3}\right)\left(\frac{\rho_s}{\rho_w}\right)^{0.25}\left(\frac{V_s}{b_s h^2}\right)^{0.5}\left(\frac{r}{h}\right)^{-2/3} \quad (6)$$

where α is the slope angle, ρ_s, ρ_w are the slide and water densities, respectively, and the same remaining parameters. The predictive equation for the maximum wave height by *Huber and Hager* [1997] is dependent mainly on the slide volume without accounting for the effects of slide Froude number, relative thickness and width at the impact. Further the radial decay rate of the height is independent of the slide impact characteristics. This results in over prediction of the maximum wave height compared with the measured maximum wave heights except in highly supercritical cases and causes the comparison to scatter widely as shown in Figure 11b. The empirical formula of *Huber and Hager* [1997] for 2-D landslide-generated tsunami waves also overestimate the measured wave heights in the direction of the slide motion ($\theta = 0°$) except in highly supercritical cases. *Fritz et al.* [2009] found that the empirical formula of *Huber and Hager* [1997] for 2-D impulse wave characteristics underestimates the wave height by a factor of 1.8 at Lituya Bay in 1958 given a highly supercritical landslide impact at Froude number F = 3.2. Rough estimations of slide thickness from photos [*Huber*, 1980] indicate that Huber's slides at comparable impact Froude numbers were thinner $s < h$ [*Fritz et al.*, 2004]. In the "Sturzbahn" channel setup higher impact velocities were attained by releasing the granular mass from higher launch positions resulting in decreasing granular slide thickness with increasing impact velocity. Controversial remains that both the 2-D and the 3-D empirical wave height predictions lack any slide impact velocity or slide duration parameter, whereas all other experimental studies confirmed the dominant influence of the slide Froude number F on the generated wave height.

[17] Comparisons of the measured wave amplitudes along the direction of the slide motion $\theta = 0°$ with some of the notable 2-D experiments result in amplitude estimates deviating within 40% to 200% of the measured values. The empirical equations given by *Kamphuis and Bowering* [1970], *Walder et al.* [2003] (solid block landslide models) and *Fritz et al.* [2004] (granular landslide model) result in overprediction of the measured wave heights. In contrast to previous 3-D studies the present study characterizes the radial amplitude attenuation rates depending on the slide impact parameters. Further, different parts of the wave train display varying attenuation behaviors.

6.3. Wave Celerity

[18] The determination of tsunami arrival times is critically important to issue and cancel tsunami warnings as well as for evacuation efforts. The arrival times can be determined by raypaths and wave propagation celerity. The linear wave propagation velocity can be determined by the wavelength λ, or the wave period T and the water depth h from the linear dispersion relation. However, the linear wave theory is valid for $a_c/h < 0.03$ [*Dean and Dalrymple*, 1991]. In the present experiments, the measured waves are in the range $0.001 < a_c/h < 0.35$. While the near field waves are in the

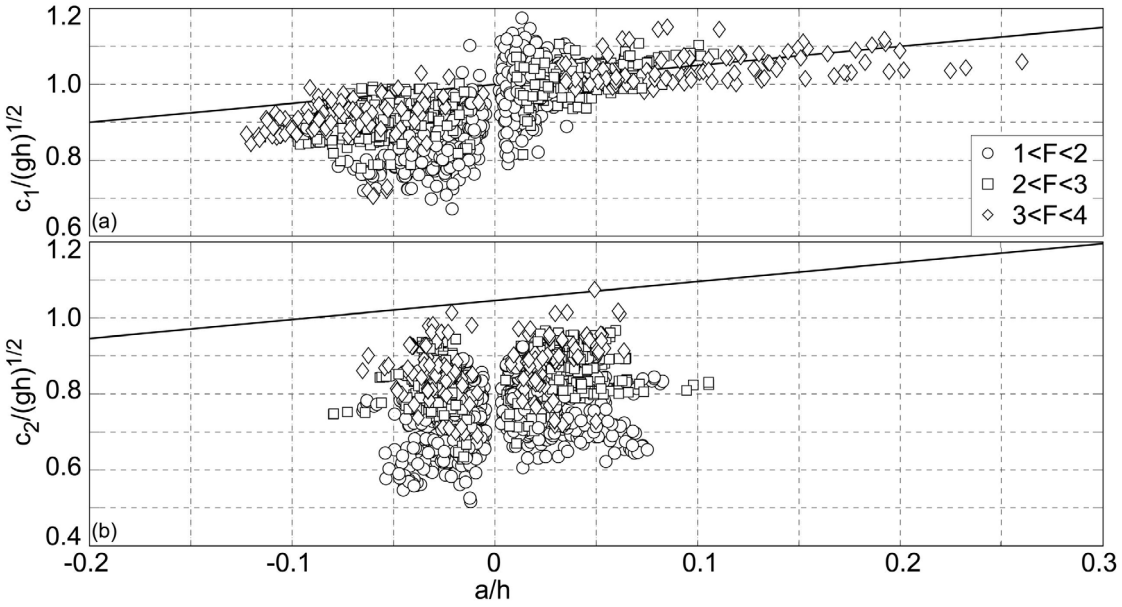

Figure 12. Wave crest and trough propagation velocities for (a) first wave and (b) second wave. Solitary wave speed approximation given by equation (7) is shown as dashed line in the figures. The trough velocities are indicated by negative relative wave amplitudes.

nonlinear regime, some basin wide waves fall into the linear wave regime. In the nonlinear regime, the wave propagation velocity further depends on the relative wave amplitude a/h or the relative wave height H/h. The increasing of both relative wavelength λ/h and Ursell number with large relative amplitudes tends to place the waves in the intermediate to shallow water depth wave regimes [*LeMéhauté*, 1976; *LeMéhauté and Wang*, 1995]. This leads to an increase in the importance of the higher-order effects on the wave train properties. The individual crests and troughs of the landslide-generated tsunami waves have independent wavelengths and propagate with different celerities. Hence, landslide-generated tsunami waves are unsteady in a reference frame moving at the wave celerity, in contrast to the solitary or cnoidal wave theories. Subsequently, each component of the generated waves is treated independently.

[19] The wave gauges were positioned in the tsunami wave basin along rays starting at 0° corresponding to the direction of the landslide motion. The successive angles of the wave gauge rays were 5°, 13°, 25°, 30°, 45°, 60° and 90°. The wave celerity is measured over the propagation range $1.67 < r/h < 78.65$ for the experimental trials and along directional rays. The tsunami wave celerity is determined for individual wave crests and troughs along directional rays based on wave gauge spacings and wave travel times. The celerity measurements are limited to wave gauge recordings prior to the arrival of wave reflections from the basin sidewalls, which primarily affect later trailing waves. Celerity measurements are made for the crests and troughs of the first three waves, which are the highest and the most important for hazard mitigation in the near field. The first wave propagation velocities are determined to $0.8 < c_{c1}/\sqrt{gh} < 1.2$ and $0.7 < c_{t1}/\sqrt{gh} < 1.0$ and accordingly for the second wave to $0.65 < c_{c2}/\sqrt{gh} < 0.97$ and $0.54 < c_{t2}/\sqrt{gh} < 0.94$ and the third wave to $0.5 < c_{c3}/\sqrt{gh} < 0.93$ and $0.5 < c_{t3}/\sqrt{gh} < 0.92$. The decrease in the propagation velocity from the leading wave to the trailing waves is due to the continuous reduction of the wavelengths from the front to the back of the wave train. The first trough propagates up to 17% slower than the first wave crest. The celerity of the second wave was on average 18%–23% lower than the leading wave celerity. The third wave was on average 22%–35% slower than the leading wave. In some experimental runs with large F and S the measured celerity of the leading wave crest exceeded by 20% the linear shallow water depth wave celerity $c = \sqrt{gh}$.

[20] The instantaneous wave celerity of the leading wavefront can be approximated by the speed of the solitary wave

$$\frac{c_{c1}}{\sqrt{gh}} = 1 + \frac{a_{c1}}{2h} \tag{7}$$

where $a_{c1} = H$ for a solitary wave [*Boussinesq*, 1872; *Laitone*, 1960]. This theoretical solution can be approximated by

$$\frac{c_{c1}}{\sqrt{gh}} = \sqrt{1 + \frac{a_{c1}}{h}} \tag{8}$$

for small relative wave crest amplitudes, a_{c1}/h [*Russell*, 1844] and represents an approximation to the theoretical studies of *Boussinesq* [1872] and *Rayleigh* [1876]. Equations (7) and (8) further compare well with experimental observations of *Dailey and Stephan Jr.* [1953] and *Naheer* [1978a, 1978b]. The breaking limit for solitary waves was given by *McCowan* [1894] as $H_b/h = 0.78$. Hence the theoretical relationships given by equations (7) and (8) increase wave celerities because of nonlinearity at breaking by up to 39% and 33% beyond the linear shallow water assumption of $c = \sqrt{gh}$. This may lead to surprising early arrivals of tsunami waves compared to estimates based solely on linear long wave theory.

[21] The measured propagation velocities of the first two landslide-generated tsunami waves are shown in Figure 12. The wave velocities are normalized by the linear shallow

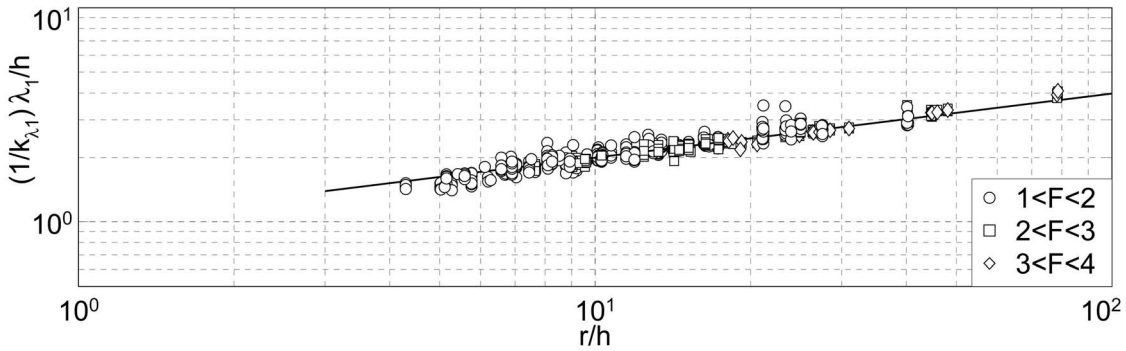

Figure 13. Measured wavelength as function of propagation distance r/h for first landslide-generated tsunami wave. The wavelength coefficient is $k_{l1} = 4.3F^{0.22}S^{0.06}L^{0.03}$.

water velocity. The velocity of the leading wave crest and trough corresponds closely to the theoretical approximation of the solitary wave speed given by equation (7). The amplitude dispersion quantified by the relative wave amplitude plays an important role in the variation of leading wave crest and trough velocities. The crest and trough of the second wave propagate at significantly lower celerities compared to the leading wave. The drop in wave celerity from the leading wave to the second wave averages 23% for the wave crest and 18% for the wave trough. The second waves propagate at speeds lower than the linear shallow water velocity $\sqrt{gh}$. These waves are typically in the intermediate water depth regime and often nonlinear near the source. The celerity of the third wave is lower than the celerity of the first two waves. Hence, neither linear wave theory nor solitary wave theory can be applied to approximate the trailing waves, which are commonly in the intermediate to deep water regime and often nonlinear near the source. The reduction in the wave celerity is attributed to the decreasing wave lengths from the front to the back of the wave train resulting in frequency dispersion.

6.4. Wave Periods and Lengths

[22] Individual wave periods are measured from the wave profiles by the zero upcrossing and crest-to-crest techniques. The initial upcrossing point is defined as the locations when the water surface elevation reaches 5% of the first wave crest amplitude, $\eta = 0.05a_{c1}$. The measured periods are wave periods of the radial wavefronts at location (r, θ). While the first two wave periods are measured in all the trials, the third wave period measurements were limited by reflections in some cases. The wave periods are measured in the range $4 < r/h < 80$, $0^\circ < \theta < 90^\circ$. The measured radial wavefront periods have a nearly constant wave period independent of the angular direction. The wave periods increase with the radial propagation distance r/h because of frequency dispersion within a wave train with continuously decreasing wave speeds from the first to the last wave. The measured first wave periods are within $6 < T_1\sqrt{g/h} < 26$ and the first crest to second crest wave periods within $5 < T_{c1}\sqrt{g/h} < 18$. On average, the first crest to second crest wave period is 18% shorter than the upcrossing wave period of the first wave. The wave periods of the second and third wavefront are in the range $3.5 < T_2\sqrt{g/h} < 10.5$ and $2 < T_3\sqrt{g/h} < 10$. There are only minor differences between the upcrossing period T_2 and second crest to third crest wave period. The little to no variation indicates the presence of an oscillatory type of trailing wave with minor nonlinear effects.

[23] The wave periods in the present study are independent of the propagation direction and are dependent on the landslide parameters at impact. Multivariable regression analysis for the first and second wave periods resulted in the following parametric equations

$$T_1\sqrt{\frac{g}{h}} = 4.8F^{0.21}S^{0.05}L^{0.04}R^{0.3} \tag{9a}$$

$$T_2\sqrt{\frac{g}{h}} = 3.0F^{0.03}S^{0.03}L^{0.01}R^{0.25} \tag{9b}$$

with correlation coefficients of 0.97 and 0.93, and maximum deviation of $\pm 14\%$ and $\pm 21\%$, respectively. The dominant variable is the slide Froude number at impact with minor dependencies on the landslide shape. The Froude number is the dominant landslide source parameter, while the relative radial propagation distance R is dominant in terms of the wave propagation and dispersion.

[24] The wavelengths are defined from upcrossing-to-upcrossing points by multiplying the wave periods with the corresponding wave speeds. In general, the wavelengths are measured as

$$\frac{\lambda_i}{h} = T_i\sqrt{\frac{g}{h}}\frac{c_i}{\sqrt{gh}} \tag{10}$$

[25] The wavelengths determined in the range $4 < r/h < 80$ and $0^\circ < \theta < 90^\circ$. are found to be $5 < \lambda_1/h < 24$ and $3 < \lambda_{c1}/h < 18$ for the first upcrossing-to-upcrossing and crest-to-crest wavelengths, respectively. The wavelengths are widely independent of the angular direction and are found to increase with propagation distance from the landslide source in accordance with the wave periods. The increasing wavelengths with propagation distance are shown in Figure 13. The tsunamis generated by three-dimensional landslides propagate as a wavefront in the radial direction with nearly constant wave periods and wavelengths with respect to the

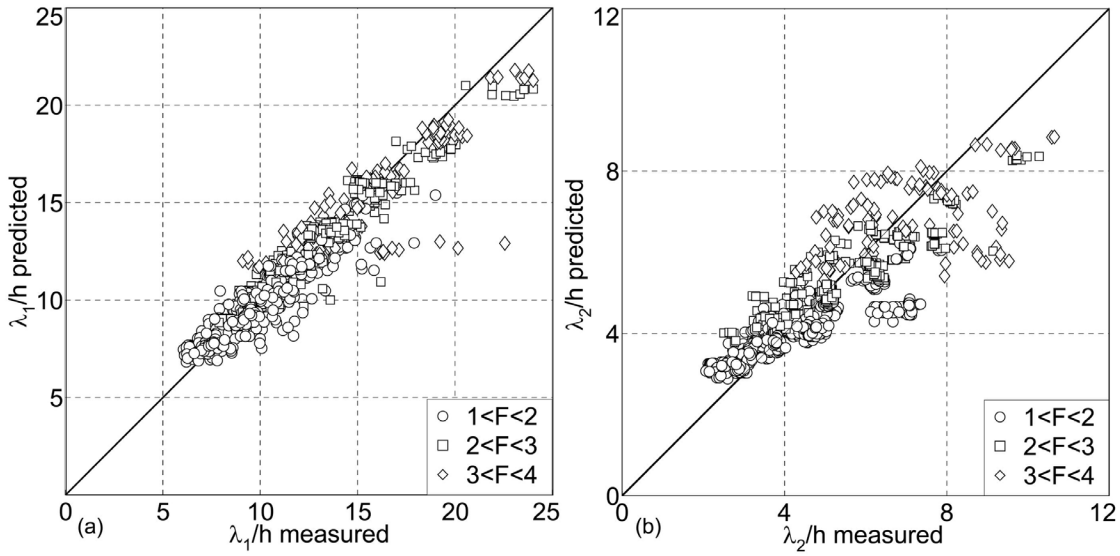

Figure 14. Comparison between measured and predicted values of upcrossing wavelengths for (a) first wave with equation (11a) and (b) second wave with equation (11b).

angular direction at constant water depth. The wavelengths for the second wave are determined to $2 < \lambda_2/h < 11$ and $2.5 < \lambda_{c2}/h < 12$. Multivariable regression analysis for the first and second wavelengths resulted in the prediction equations

$$\frac{\lambda_1}{h} = 4.3F^{0.22}S^{0.06}L^{0.03}R^{0.3} \tag{11a}$$

$$\frac{\lambda_2}{h} = 2.0F^{0.22}S^{0.04}L^{0.07}R^{0.25} \tag{11b}$$

with correlation coefficients of 0.95 and 0.86, and maximum deviation of ±10% and ±17%, respectively. The dominant parameters are again the slide Froude number at impact and the relative radial propagation distance R. The comparisons between the measured and predicted values of the first two upcrossing-to-upcrossing wavelengths by equations (11a) and (11b) are shown in Figure 14.

6.5. Wave Nonlinearity

[26] The wave nonlinearity can be defined by relative wave height H/h or amplitude a/h, wave steepness H/λ and Ursell number $U = (a_c\lambda^2)/h^3$ depending upon the water depth regime [*Ursell et al.*, 1960]. In the shallow water depth wave regime, relative wave height or amplitude is important while in the deep water regime, the most relevant parameter is the wave steepness. In intermediate water depths, the Ursell number represents a combination of the former two parameters, which may be considered. Most of the generated waves are in the intermediate water depth regime with $2 < \lambda/h < 20$. The measured amplitudes in the present study are in the range $0.001 < a_{c1}/h < 0.2$. Some of the generated waves are in the weakly nonlinear regime with nonlinearity decreasing rapidly away from the tsunami generation area. The wave propagation velocity is affected by the amplitude dispersion in the near field. The wave steepness and the Ursell number are determined over the range $5 < r/h < 80$ in the experiments. The wave steepness decreases with the propagation distance in accordance with a simultaneous decay in amplitude and increase in wavelength with propagation distance. The wave steepness of the leading wave is in the range $6 \times 10^{-4} \le H_1/\lambda_1 \le 0.025$. The condition for linear theory with $H/\lambda \le 0.006$ places some of the generated waves into the nonlinear regime [*Dean and Dalrymple*, 1991]. Landslide-generated tsunami waves are often in the intermediate water depth regime where the Ursell number is the preeminent criteria. The Ursell number for the first wave is in the range $0.2 < U_1 < 55$ placing most generated waves in the nonlinear regime with $U > 1$ in the intermediate water depth regime [*Lighthill*, 1978]. The wave steepness for the second wave is in the range $0.0015 < H_2/\lambda_2 < 0.075$. The wave steepness of the second wave in the generated wave train is larger than the first wave because of shorter second wavelengths. Second wave Ursell numbers are in the range $0.02 < U_2 < 4$. The second waves are linear in the far field where the amplitude decay and dispersion effects lead to $U_2 < 1$. For the third wave, the wave steepness and Ursell numbers are within $0.002 < H_3/\lambda_3 < 0.06$ and $0.007 < U_3 < 2$.

7. Energy Conversion

[27] The energy conversion is estimated between the landslide kinetic energy and the generated tsunami waves. The kinetic energy of the landslide at impact may be given as $E_s = \frac{1}{2}\rho_s V_s v_s^2$ where ρ_s is the landslide density, V_s is the landslide volume and v_s is the landslide velocity at impact. The wave potential energy per unit width of the wavefront from the wave profiles measurements is determined as

$$dE_{pot} = \frac{1}{2}\rho_w g c \int_0^T \eta^2 dt \tag{12}$$

[28] In a three-dimensional cylindrical coordinate system, since the wave propagates as a radial wavefront, the measured

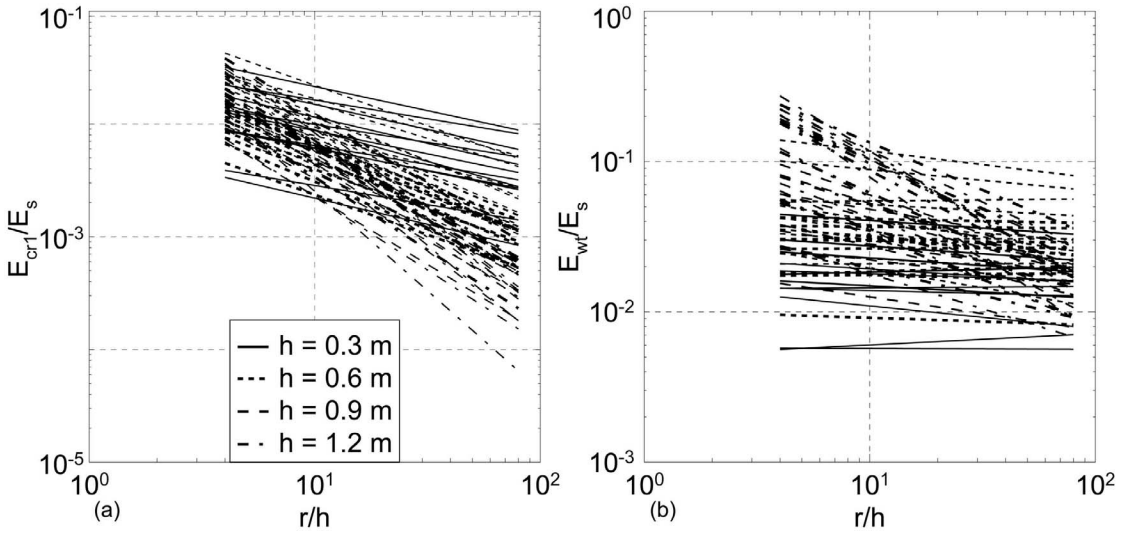

Figure 15. Decay of wave energy relative to landslide kinetic energy at impact with propagation distance for (a) first wave crest E_{cr1}/E_s and (b) wave train E_{wt}/E_s.

energy from equation (12) is a function of propagation distance and direction, $dE_{pot}(r, \theta)$. The total potential energy of the wavefront at propagation distance r is computed as

$$E_{pot} = \int_{-\pi/2}^{\pi/2} \left(\frac{1}{2} \rho_w g c \int_0^T \eta^2 dt \right) r d\theta \tag{13}$$

at a propagation distance r from the landslide source. The integration range spans from zero to the first down crossing point when the energy of the leading wave crest is considered. For computing the wave train energy, the range 0 to T_3 is considered in the present experiments. The measured unit potential energy at locations (r, θ) are approximated as $dE_{pot} = f(r, \theta)$ which enables the interpolation of the energy measurements in the wave propagation range in the wave basin $0 \le r \le r_{\max}$ and $-\pi/2 \le \theta \le \pi/2$, where $r_{\max} = 24$ m is the location of the farthest wave gauge in the wave basin. The interpolation function for the wave potential energy for the leading wave crest was obtained as

$$dE_{pot}(r, \theta) = k_{Ec1}(r)^n \cos^2 \theta \tag{14}$$

where k_{Ec1} is the generation mechanism and the decay rate, n is analogous to the amplitude decay rate. Then the total crest potential energy is measured by using equation (14). This expression represents the potential wave energy per unit width for a certain generation mechanism. The kinetic energy of the generated waves is difficult to estimate directly because of lack of measured water particle kinematics in the water column. The total wave energy may be estimated as $E_{tot} \approx 2E_{pot}$ by assuming equipartition of energy between potential and kinetic wave energy for linear waves [*Lamb*, 1932]. The total wave energy $E_{tot} = E_{pot} + E_{kin}$ computed numerically may exceed total wave energy estimates based on equipartition by up to 11% for a solitary wave approaching breaking height, but is typically only a few percent in the present study [*Williams*, 1985]. The accuracy of potential wave energy estimates computed according to equation (12) is limited to roughly ±15% because of the assumption of a constant wave propagation velocity c of individual crests and troughs. The accuracy of the wave energy estimates may further decay for breaking waves. The energy of the leading wave crest was found to decrease with the propagation distance attributed to dispersion of the wave energy and migration through the tsunami wave train. The bulk of the wave train energy is captured by summing up the wave energy contained in the first three waves. The energy decays of the leading wave crest and the wave train are shown in Figures 15a and 15b. The decay rates are influenced by the energy transfer from the landslide to the generated waves, the water depth regime and the nonlinearity of the generated waves. In some cases, the decay of the leading crest energy is rapid with $E_{cr1}(r/h = 6)/E_{cr1}(r/h = 4) = 0.5$ for intermediate water depth regime, while in some cases the decay is more gradual with $E_{cr1}(r/h = 32)/E_{cr1}(r/h = 4) = 0.5$ in shallow water depth cases. The energy decay in the leading wave crest is due to the dispersion of the waves in the intermediate water depth regime and transfer of energy to the trailing waves in the wave train [*Løvholt et al.*, 2008]. The decay rate in general is lower for the wave train compared with the leading wave crest energy. The decay rate for the leading wave crest varies with the efficiency of the wave generation, the type of the generated wave, dispersion effects and the rate of energy transfer from the front toward the back of the wave. The energy decay rate for the wave train varies with wave generation efficiency and energy transfer during propagation because of dispersion effects. The multivariable regression analysis for the leading wave crest energy in terms of the landslide parameters yields

$$\frac{E_{cr1}\left(\frac{r}{h} = 10\right)}{E_s} = 0.02 S^{0.9} F^{0.7} V^{-0.1} \tag{15}$$

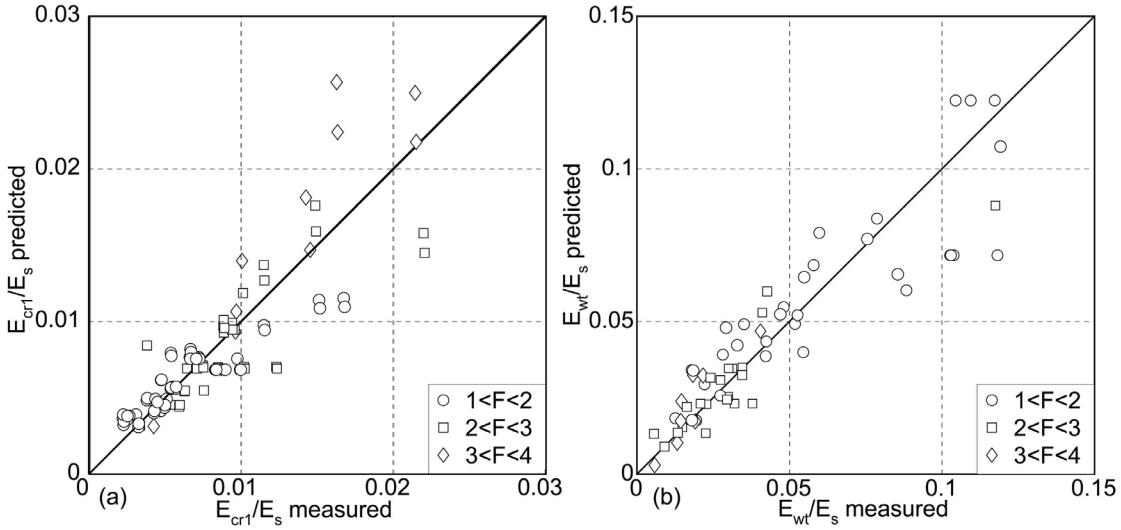

Figure 16. Comparison between measured and predicted wave energy conversion for (a) leading wave crest E_{cr1}/E_s computed with equation (15) and (b) wave train energy E_{wt}/E_s computed with equation (16).

with correlation coefficient of 0.86 and maximum deviation of ±25%. Between 0.5 and 4% of slide energy is transferred to the leading wave crest energy. The wave train energy is found to be

$$\frac{E_{wt}\left(\frac{r}{h}=10\right)}{E_s} = 0.13SF^{0.8}V^{-0.7} \tag{16}$$

with correlation coefficient of 0.89 and maximum deviation of ±19%. Between 1 and 15% of the landslide energy is converted into the wave train energy. The comparison between the measured and predicted energy conversion rates for the leading wave crest and the wave train is shown in Figures 16a and 16b. The wave generation efficiency of granular landslides increases with decreasing relative landslide volumes V, increasing relative landslide thickness S and slide Froude number F at impact. The energy partition between the leading wave crest and wave train is obtained in terms of landslide parameters as

$$\frac{E_{c1}\left(\frac{r}{h}=10\right)}{E_{wt}\left(\frac{r}{h}=10\right)} = 0.125F^{0.3}V^{0.6} \tag{17}$$

with correlation coefficient of 0.89 and maximum deviation of ±21%. Increasing relative landslide volume and Froude number at impact increases the efficiency of wave generation. With increasing effectiveness of impact, a larger percentage of the total available energy is converted into the leading wave crest compared with the rest of the wave train. The ratio of the leading wave crest energy with the solitary wave energy with the same amplitude was in the range 15–75%. The limits corresponds to extreme cases of slow and thin landslides versus fast and thick landslides. The two-dimensional granular slide experiments conducted by *Huber* [1980] yielded slide impact energy to wave energy conversions between 1 and 40%. *Huber* [1980] and *Panizzo et al.* [2005] do not provide energy conversion rates for their 3-D experiments. The 2-D granular landslide studies by *Fritz et al.* [2004] measured 2% to 30% energy conversion from the granular landslide to the leading wave crest at a distance $x/h = 8$ from the impact. The corresponding energy conversion into the first three crests of the wave train was within 4% to 50% at the same location. These flume experiments provided a comparison between the leading wave energy and the energy of a solitary wave with the same characteristics. *Watts* [2000] studied submarine landslide blocks as tsunami source in a 2-D flume with energy conversion rates between 2% and 13%. The 2-D studies by *Ataie-Ashtiani and Nik-Khah* [2008] observed an energy conversion rate between 5% and 50% with varying solid block landslides as the source of the wave generation. *Heller and Hager* [2010] measured energy conversion rates between 11.3% and 85.7% for 2-D granular landslides. The present 3-D study yields lower energy conversion rates when compared with 2-D flume experiments of *Kamphuis and Bowering* [1970], *Huber* [1980], *Fritz et al.* [2004], *Heller and Hager* [2010], and *Ataie-Ashtiani and Nik-Khah* [2008]. In general, energy conversion rates in the present study were significantly lower than 2-D and 3-D block studies. The 2-D experiments result in efficient tsunami wave generation by landslide as only the vertical plane is unconfined allowing landslide motion and water body displacement. Further, since the energy is proportional to surface elevation squared which results in higher-energy conversion rates in 2-D compared with 3-D. In comparison, there is no lateral confinement of both the deformable landslide and water body in 3-D. During the landslide impact, the water body can escape laterally and flow around the landslide which decreases the efficiency of wave generation. The landslide deformation is larger in 3-D compared with 2-D because of the lack of lateral constraint on the landslide motion. The additional degree of freedom in 3-D experiments increases granular landslide deformation, thereby reducing the effectiveness of the energy conversion and wave generation. Slide energy is lost into frictional effects during the subaerial and subaqueous motion and internal slide deformation in particular at the transition from the hillslope on to the horizontal basin bottom. Energy dissipation also decreases the energy conversion during the collapse of the impact crater. In

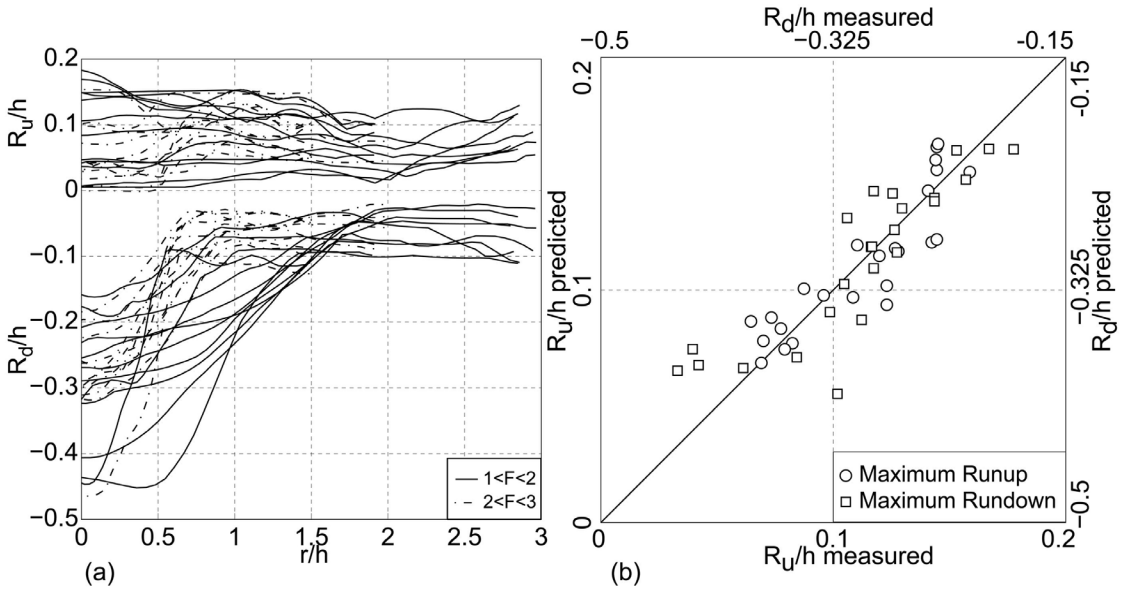

Figure 17. Maximum wave runup, R_u/h, and drawdown amplitudes, R_d/h, in the (a) landslide impact region on the hillslope in the range $0 \le r/h \le 3$ and (b) comparison between measured and predicted wave runup and drawdown at impact location.

particular, the energy lost into frictional effects and internal slide deformation varies between 2-D and 3-D landslide propagation. This results in different amount of slide energy available for conversion into the generated waves. The remaining energy is spread in the angular direction through the radial wavefront propagation. The density of the wave energy in the generated wave train disperses and decays with propagation distance.

8. Tsunami Runup and Drawdown

[29] The tsunami runup and rundown on the hillslope are measured by wave runup gauges combined with overlapping camera image recordings. Measurements are made relating to the lateral wave profiles, shoreline variation during the lateral wave propagation and extents of maximum runup and drawdown of the shoreline on the hillslope. The maximum runup and drawdown in the impact region is shown in Figure 17a. Along the hillslope, the maximum runup and drawdown occurs at the impact location, $r/h = 0$. In the impact region, the shoreline draws down initially because of the granular landslide impact with the water surface, followed by a wave runup on the hillslope. The maximum tsunami runup and drawdown may be directly related to the initial landslide impact at the water surface, governed primarily by the landslide Froude number F and thickness S at impact. Secondarily it is influenced by landslide volume and width at impact. The empirical equations obtained for the maximum runup and drawdown at impact are

$$\frac{R_u}{h} = \frac{1}{4} F^{1.4} S^{0.7} B^{-0.5} V^{-0.1} \tag{18a}$$

$$\frac{R_d}{h} = \frac{2}{5} F^{1.8} S^{0.3} B^{-1.2} V^{-0.2} \tag{18b}$$

with correlation coefficient $r^2 = 0.89$ and maximum deviation of $\pm 24\%$ for both the runup and drawdown. The comparison between the measured and predicted values of the wave runup and drawdown in the impact region is shown in Figure 17b. The maximum drawdown exceeds the maximum runup in case of subaerial landslide impacts in the present experiments. The runup and drawdown on the hillslope decreases with the propagation distance.

[30] The lateral tsunami wave period on the hillslope is measured in the range $0 < r/h < 20$. The determined wave periods are within the range $10 < T\sqrt{g/h} < 20$, which coincides with the measured range of the offshore propagating tsunami waves. The wave period increases with the propagation distance similarly to the offshore propagating waves, demonstrating an $(r/h)^{0.3}$ dependency. A similar behavior is seen in the lateral wavelength, measured in the range $0 < r/h < 20$. The measured lateral wavelengths are found in the range $2.5 < \lambda/h < 12$, in comparison, the offshore propagating wavelengths are measured in the range $5 < \lambda/h < 15$. The lateral wavelengths are shorter than the offshore propagating waves because they propagate in shallower water depths. Since the landslide motion is primarily unidirectional, the wave maker characteristics and the generation mechanism further affect the length of the lateral waves. Further, the difference between longitudinal and transverse length and time scales for the slide propagation adds to the difference in the generation mechanism of the offshore propagating waves versus the lateral propagating waves.

[31] The measured wave periods and lengths for the first lateral wave correspond to the zeroth mode of the edge wave dispersion relation given by *Ursell* [1952]

$$\omega^2 = g k_y \sin(2n+1)\alpha \tag{19}$$

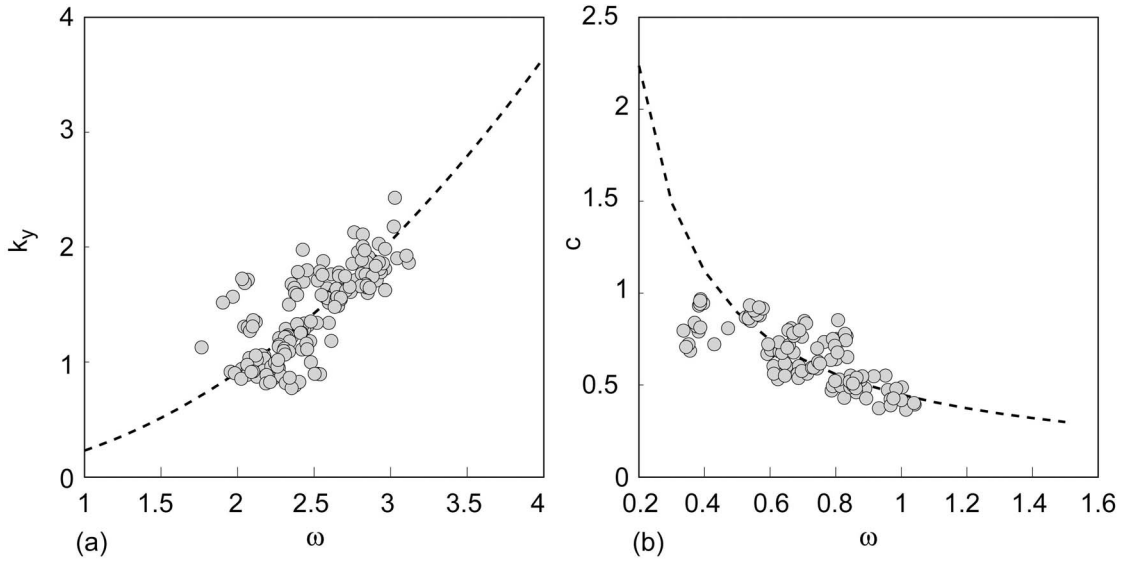

Figure 18. Edge wave dispersion: (a) comparison of measured wave number and frequency with the zeroth mode edge wave dispersion relation (equation (19)); (b) measured wave celerity as a function of wave frequency compared with edge wave dispersion relation (dashed line) given by *Ursell* [1952].

with $n = 0$, where ω is the frequency and k_y is the wave number corresponding to the lateral tsunami waves, g is the gravitational acceleration and α is the hillslope angle. The comparison between the measured wave parameters and zeroth mode dispersion relation is shown in Figure 18a.

[32] The speed of the lateral wave is measured for the first two waves on the hillslope in the propagation range $0 < r/h < 20$. The propagation velocity of the first wave is in the range $0.35 < c_{c1}/\sqrt{gh} < 1$ and $0.35 < c_{t1}/\sqrt{gh} < 1$. The measured wave celerity versus the edge wave frequency is shown in Figure 18b along with the zeroth mode edge wave dispersion relation. The second wave speed is measured in the range $0.35 < c_{c2}/\sqrt{gh} < 0.85$ and $0.3 < c_{t1}/\sqrt{gh} < 0.85$. The reduction in the wave speed from the first to the second lateral wave may be due to the dispersion effects similar to the offshore propagating wave.

9. Conclusions

[33] Tsunamis generated by three-dimensional deformable granular landslides are physically modeled based on the generalized Froude similarity. The pneumatic landslide tsunami generator controlled the individual landslide parameters at impact, thus enabling to study wave generation and propagation across a wide range of landslide parameters in various water depth regimes. The wave generation is influenced by the nondimensional landslide parameters at impact such as the Froude number F, thickness S, width B and length L_s. Additionally, the relative landslide volume V affects the wave generation. Three-dimensional landslide-generated tsunami waves travel as radial wavefronts away from the impact region. Recorded wave profiles were either nonlinear oscillatory or nonlinear transition type of waves depending primarily on the slide Froude number F or thickness S at impact. The leading wave crest amplitudes are mainly dependent on the landslide Froude number F and thickness S at impact, while the length of the slide additionally affects the leading wave trough and trailing waves. The amplitude attenuation additionally depends on the landslide width at impact. The angular decay rate of the trailing wave is faster than the leading waves. Wave periods and wavelengths are widely independent of the angular direction and increase with propagation distance. The propagation velocity of the leading wave crest corresponds closely to the theoretical approximation of the solitary wave speed while the trailing waves are slower owing to dispersion effects. Three-dimensional landslides are less efficient wave generators compared with two-dimensional cases, because of the increased landslide deformation in 3-D compared with 2-D and the spread of the unidirectional landslide energy across the radial wavefront. Between 1 to 15% of the landslide kinetic energy is converted into the wave train. The leading wave crest captures between 8 to 60% of the wave train energy contained in the first three waves. The wave generation efficiency increases with increasing landslide Froude number F and relative landslide thickness S at impact. However, the efficiency decreases with increasing volume V by increasing the relative landslide length L_s. The recorded 3-D landslide-generated tsunami waves are mostly weakly nonlinear in nature and may span from shallow to deep water depth regimes within a generated wave train. Directly applying the empirical equations given by another three dimensional solid block landslide study to the present experiments on granular landslide-generated tsunamis results in a wave height underestimation by a factor of two, which may be attributed to differences in landslide runout duration. While an earlier empirical equation for the three-dimensional granular landslide tsunami height scatters widely in comparison and provides a poor correlation when applied to the present experimental data. This unique experimental data on tsunamis generated by three dimensional deformable granular landslides serves validation of numerical models.

[34] **Acknowledgments.** This research is supported by the National Science Foundation (NSF) through grants CMMI-0421090, CMMI-0936603, CMMI-0402490, and CMMI-0927178. Support by the scientific personnel and technical staff at the O. H. Hinsdale wave research laboratory, Oregon State University, Corvallis, OR, and the Network of Earthquake Engineering Simulation (NEES) is acknowledged. The comments and insights provided by Carl B. Harbitz and the two anonymous reviewers are greatly appreciated.

References

Ataie-Ashtiani, B., and A. Najafi-Jilani (2008), Laboratory investigations on impulse waves caused by underwater landslides, *Coastal Eng.*, *55*, 989–1074, doi:10.1016/j.coastaleng.2008.03.003.

Ataie-Ashtiani, B., and A. Nik-Khah (2008), Impulsive waves caused by subaerial landslides, *Environ. Fluid Mech.*, *8*, 263–280, doi:10.1007/s10652-008-9074-7.

Bardet, J.-P., C. Synolakis, H. Davis, F. Imamura, and E. A. Okal (2003), Landslide tsunamis: Recent findings and research directions, *Pure Appl. Geophys.*, *160*, 1793–1809, doi:10.1007/s00024-003-2406-0.

Bondevik, S., F. Løvholt, C. Harbitz, J. Mangerud, A. Dawson, and J. Svendsen (2005), The Storegga slide tsunami comparing field observations with numerical solutions, *Mar. Pet. Geol.*, *22*, 195–208, doi:10.1016/j.marpetgeo.2004.10.003.

Boussinesq, J. (1872), Théorie des ondes et des remous que se propagent le long d'un canal rectangulaire horizontal, en communiquant au liquide contenu dans ce canal des vitesses sensiblement pareilles de la surface au fond, *J. Math. Pures Appl.*, *17*, 55–108.

Dailey, J. W., and S. C. Stephan Jr. (1953), Characteristics of the solitary wave, *Trans. Am. Soc. Civ. Eng.*, *118*, 575–587.

Dean, R. G., and R. A. Dalrymple (1991), *Water Wave Mechanics for Engineers and Scientists, Advanced Series on Ocean Engineering*, vol. 2., World Sci., Singapore.

Di Risio, M., P. DeGirolamo, G. Bellotti, A. Panizzo, F. Aristodemo, M. G. Molfetta, and A. F. Petrillo (2009), Landslide-generated tsunamis runup at the coast of a conical island: New physical model experiments, *J. Geophys. Res.*, *114*, C01009, doi:10.1029/2008JC004858.

Enet, F., and S. T. Grilli (2005), Tsunami landslide generation: Modelling and experiments, paper 88 presented at Fifth International Symposium on Ocean Wave Measurement and Analysis, Cent. de Estud. y Exp. de Obras Publicas, Madrid, Spain.

Enet, F., and S. T. Grilli (2007), Experimental study of tsunami generation by three-dimensional rigid underwater landslides, *J. Waterw. Port Coastal Ocean Eng.*, *133*(6), 442–454, doi:10.1061/(ASCE)0733-950X(2007)133:6(442).

Fine, I., A. Rabinovich, B. Bornhold, R. Thomson, and E. Kulikov (2005), The Grand Banks landslide-generated tsunami of November 18, 1929: Preliminary analysis and numerical modeling, *Mar. Geol.*, *215*, 45–57, doi:10.1016/j.margeo.2004.11.007.

Fritz, H. M. (2002), Initial phase of landslide-generated impulse waves, PhD thesis, Eidg. Tech. Hochsch., Zurich, Switzerland.

Fritz, H. M., and J. C. Borrero (2006), Somalia field survey after the December 2004 Indian Ocean tsunami, *Earthquake Spectra*, *22*(S3), 219–233, doi:10.1193/1.2201972.

Fritz, H. M., W. H. Hager, and H.-E. Minor (2001), Lituya Bay case: Rockslide impact and wave run-up, *Sci. Tsunami Hazards*, *19*(1), 3–22.

Fritz, H. M., W. H. Hager, and H.-E. Minor (2003a), Landslide generated impulse waves. 1. Instantaneous flow fields, *Exp. Fluids*, *35*, 505–519, doi:10.1007/s00348-003-0659-0.

Fritz, H. M., W. H. Hager, and H.-E. Minor (2003b), Landslide generated impulse waves. 2. Hydrodynamic impact craters, *Exp. Fluids*, *35*, 520–532, doi:10.1007/s00348-003-0660-7.

Fritz, H. M., W. H. Hager and H.-E. Minor (2004), Near field characteristic of landslide generated impulse waves, *J. Waterw. Port Coastal Ocean Eng.*, *130*, 287–302, doi:10.1061/(ASCE)0733-950X(2004)130:6(287).

Fritz, H. M., F. Mohammed, and J. Yoo (2009), Lituya bay landslide impact generated mega-tsunami 50th anniversary, *Pure Appl. Geophys.*, *166*, 153–175, doi:10.1007/s00024-008-0435-4.

Fritz, H. M., J. V. Hillaire, E. Molière, Y. Wei and F. Mohammed (2012), Twin tsunamis triggered by the 12 January 2010 Haiti earthquake, *Pure Appl. Geophys.*, doi:10.1007/s00024-012-0479-3, in press.

Grilli, S. T., and P. Watts (2005), Tsunami generation by submarine mass failure. I: Modeling, experimental validation, and sensitivity analyses, *J. Waterw. Port Coastal Ocean Eng.*, *131*, 283–297, doi:10.1061/(ASCE)0733-950X(2005)131:6(283).

Hammack, J. L. (1973), A note on tsunamis: Their generation and propagation in an ocean of uniform depth, *J. Fluid Mech.*, *60*, 769–799, doi:10.1017/S0022112073000479.

Hampton, M. A., H. J. Lee, and J. Locat (1996), Submarine landslides, *Rev. Geophys.*, *34*(1), 33–59, doi:10.1029/95RG03287.

Harbitz, C. B., G. Pedersen, and B. Gjevik (1993), Numerical simulations of large water waves due to landslides, *J. Hydraul. Eng.*, *119*(12), 1325–1342, doi:10.1061/(ASCE)0733-9429(1993)119:12(1325).

Heinrich, P. (1992), Nonlinear water waves generated by submarine and aerial landslides, *J. Waterw. Port Coastal Ocean Eng.*, *118*(3), 249–266, doi:10.1061/(ASCE)0733-950X(1992)118:3(249).

Heller, V., and W. H. Hager (2010), Impulse product parameter in landslide generated impulse waves, *J. Waterw. Port Coastal Ocean Eng.*, *136*(3), 145–155, doi:10.1061/(ASCE)WW.1943-5460.0000037.

Heller, V., and R. D. Kinnear (2010), Discussion on "Experimental investigation of impact generated tsunami; related to a potential rock slide, Western Norway" by G. Sælevik, A. Jensen, G. Pedersen [*Coastal Eng. 56* (2009) 897–906], *Coastal Eng.*, *57*, 773–777, doi:10.1016/j.coastaleng.2010.02.008.

Huber, A. (1980), Schwallwellen in Seen als Folge von Bergstürzen, *VAW Mitteil. 47*, Versuchsanst. fuer Wasserbau, Hydrol. und Glaziol., ETH Zurich, Zurich, Switzerland.

Huber, A., and W. H. Hager (1997), Forecasting impulse waves in reservoirs, *Rep. XIX*, pp. 993–1005, Comm. Int. des Grands Barrages, Rio de Janeiro, Brazil.

Hughes, S. (1993), *Physical Models and Laboratory Techniques in Coastal Engineering*, *Adv. Ser. Ocean Eng.*, vol. 7, World Sci., Singapore.

Iverson, R. M., M. Logan, and R. P. Denlinger (2004), Granular avalanches across irregular three-dimensional terrain: 2. Experimental tests, *J. Geophys. Res.*, *109*, F01015, doi:10.1029/2003JF000084.

Jørstad, F. (1968), Waves generated by landslides in Norwegian fjords and lakes, *Norw. Geotech. Inst. Publ.*, *79*, 13–32.

Kamphuis, J. W., and R. J. Bowering (1970), Impulse waves generated by landslides, paper presented at Twelfth Coastal Engineering Conference, Coastal Eng. Res. Counc., Washington, D. C.

Laitone, E. V. (1960), The second approximation to cnoidal and solitary waves, *J. Fluid Mech.*, *9*, 430–444, doi:10.1017/S0022112060001201.

Lamb, H. (1932), *Hydrodynamics*, 6th ed., Dover, New York.

Law, L., and A. Brebner (1968), On water waves generated by landslides, paper 2561 presented at Third Australasian Conference on Hydraulics and Fluid Mechanics, Sydney, N. S. W., Australia.

LeMéhauté, B. (1976), *An Introduction to Hydrodynamics and Water Waves*, Springer, New York.

LeMéhauté, B., and S. Wang (1995), *Water Waves Generated by Underwater Explosions*, *Adv. Ser. Ocean Eng.*, vol. 10, World Sci., Singapore.

Lighthill, J. A. (1978), *Waves in Fluids*, Cambridge Univ. Press, Cambridge, U. K.

Liu, P. C. (2000), Wavelet transform and new perspective on coastal and ocean engineering data analysis, in *Advances in Coastal and Ocean Engineering*, vol. 6, edited by P. L. F. Liu, pp. 57–102, World Sci., Singapore.

Liu, P. L.-F., T.-R. Wu, F. Raichlen, C. E. Synolakis, and J. C. Borrero (2005), Runup and rundown generated by three-dimensional sliding masses, *J. Fluid Mech.*, *536*, 107–144, doi:10.1017/S0022112005004799.

Løvholt, F., G. Pedersen, and G. Gisler (2008), Oceanic propagation of a potential tsunami from the La Palma Island, *J. Geophys. Res.*, *113*, C09026, doi:10.1029/2007JC004603.

McCowan, J. (1894), On the highest wave of permanent type, *Philos. Mag.*, *38*, 351–358, doi:10.1080/14786449408620643.

Miller, R. L. (1970), Prediction curves for waves near the source of an impulse, paper presented at Twelfth Coastal Engineering Conference, Coastal Eng. Res. Counc., Washington, D. C.

Mohammed, F. (2010), Physical modeling of tsunamis generated by three-dimensional deformable granular landslides, PhD thesis, Ga. Inst. of Technol., Atlanta.

Mohammed, F., and H. M. Fritz (2010), Experiments on tsunamis generated by 3D granular landslides, in *Submarine Mass Movements and Their Consequences*, *Adv. Nat. Technol. Hazards Res.*, vol. 28, edited by D. C. Mosher et al., pp. 705–718, Springer, New York.

Mohammed, F., B. C. McFall, and H. M. Fritz (2011), Tsunami generation by 3D deformable granular landslides, in *Solutions to Coastal Disasters 2011 : Proceedings of the 2011 Solutions to Coastal Disasters Conference, June 25–29, 2011, Anchorage, Alaska*, edited by L. Wallendorf et al., pp. 98–108, Am. Soc. Civ. Eng., Reston, Va.

Müller, L. (1964), The rock slide in the Vajont Valley, *Rock Mech. Eng. Geol.*, *2*, 148–212.

Müller, L. (1968), New considerations on the Vajont slide, *Rock Mech. Eng. Geol.*, *6*(1–2), 1–91.

Naheer, E. (1978a), Laboratory experiments with solitary wave, *J. Waterw. Port Coastal Ocean Eng.*, *104*(WW4), 421–436.

Naheer, E. (1978b), The damping of solitary waves, *J. Hydraul. Res.*, *16*(3), 235–249, doi:10.1080/00221687809499619.

Naranjo, J. A., M. Arenas, J. Clavero, and O. Muñoz (2009), Mass movement-induced tsunamis: Main effects during the Patagonian Fjordland

seismic crisis in Aisen (45°25′S), Chile, *Andean Geol.*, *36*(1), 137–145, doi:10.4067/S0718-71062009000100011.
Noda, E. (1970), Water waves generated by landslides, *J. Waterw. Port Coastal Ocean Eng.*, *96*(WW4), 835–855.
Ogawa, T. (1924), Notes on the volcanic and seismic phenomena in the volcanic district of Shimabara, with a report on the earthquake of December 8, 1922, *Mem. Coll. Sci., Kyoto Imp. Univ., Ser. B*, *1*(2), 3.
Okal, E. A., and C. E. Synolakis (2004), Source discriminants for near-field tsunamis, *Geophys. J. Int.*, *158*, 899–912, doi:10.1111/j.1365-246X.2004.02347.x.
Panizzo, A., G. Bellotti, and P. DeGirolamo (2002), Application of wavelet transform analysis to landslide generated waves, *Coastal Eng.*, *44*, 321–338, doi:10.1016/S0378-3839(01)00040-0.
Panizzo, A., P. DeGirolamo, and A. Petaccia (2005), Forecasting impulse waves generated by subaerial landslides, *J. Geophys. Res.*, *110*, C12025, doi:10.1029/2004JC002778.
Rayleigh, L. (1876), On waves, *Philos. Mag.*, *1*(4), 257–279.
Rickenmann, D. (1999), Empirical relationships for debris flows, *Nat. Hazards*, *19*, 47–77, doi:10.1023/A:1008064220727.
Russell, J. S. (1837), Report of the Committee on Waves, in *Report of the 7th Meeting of the British Association for the Advancement of Science*, vol. 7, pp. 417–496, Br. Assoc. for the Adv. of Sci., Liverpool, U. K.
Russell, J. S. (1844), Report on waves, in *Report of the 14th Meeting of the British Association for the Advancement of Science*, vol. 14, pp. 311–390, Br. Assoc. for the Adv. of Sci., Liverpool, U. K.
Sælevik, G. (2009), Particle image velocimetry applied to complex flows in a wave tank, PhD thesis, Dep. of Math., Univ. of Oslo, Oslo.
Sælevik, G., A. Jensen, and G. Pedersen (2009), Experimental investigation of impact generated tsunami; related to a potential rock slide, western Norway, *Coastal Eng.*, *56*, 897–906, doi:10.1016/j.coastaleng.2009.04.007.
Sander, J., and K. Hutter (1992), Evolution of weakly non-linear shallow water waves generated by a moving boundary, *Acta Mech.*, *91*(3–4), 119–155, doi:10.1007/BF01194106.
Savage, S. B. (1979), Gravity flow of cohesionless granular materials in chutes and channels, *J. Fluid Mech.*, *92*(1), 53–96, doi:10.1017/S0022112079000525.
Savage, S. B., and K. Hutter (1989), The motion of a finite mass of granular material down a rough incline, *J. Fluid Mech.*, *199*, 177–215, doi:10.1017/S0022112089000340.
Schatzmann, M., P. Fischer, and G. R. Bezzola (2003), Rheological behavior of fine and large particle suspensions, *J. Hydraul. Eng.*, *129*(10), 796–803, doi:10.1061/(ASCE)0733-9429(2003)129:10(796).
Sepúlveda, S. A., and A. Serey (2009), Tsunamigenic, earthquake-triggered rock slope failures during the April 21, 2007 Aisen earthquake, southern Chile (45.5°S), *Andean Geol.*, *36*(1), 131–136, doi:10.4067/S0718-71062009000100010.
Slingerland, R. L., and B. Voight (1979), Occurrences, properties and predictive models of landslide-generated impulse waves, in *Rockslides and Avalanches*, *Dev. Geotech. Eng.*, vol. 14B, edited by B. Voight, pp. 317–397, Elsevier, Amsterdam.
Synolakis, C. E., J. P. Bardet, J. C. Borrero, H. Davies, E. A. Okal, E. Silver, J. Sweet, and D. Tappin (2002), Slump origin of the 1998 Papua New Guinea tsunami, *Proc. R. Soc. London A*, *458*(2020), 763–789, doi:10.1098/rspa.2001.0915.
Tinti, S., A. Manucci, G. Pagnoni, A. Armigliato, and R. Zaniboni (2005), The 30 December 2002 landslide-induced tsunamis in Stromboli: Sequence of the events reconstructed from the eyewitness accounts, *Nat. Hazards Earth Syst. Sci.*, *5*, 763–775, doi:10.5194/nhess-5-763-2005.
Tinti, S., A. Maramai, A. Armigiliato, L. Graziani, A. Manucci, G. Pagnoni, and F. Zanoboni (2006), Observations of physical effects from tsunamis of December 30, 2002 at Stromboli volcano, Southern Italy, *Bull. Volcanol.*, *68*, 450–461, doi:10.1007/s00445-005-0021-x.
Ursell, F. (1952), Edge waves on a sloping beach, *Proc. R. Soc. London A*, *214*(1116), 79–97, doi:10.1098/rspa.1952.0152.
Ursell, F., R. G. Dean, and Y. S. Yu (1960), Forced small-amplitude water waves: A comparison of theory and experiment, *J. Fluid Mech.*, *7*, 33–52, doi:10.1017/S0022112060000037.
Voight, B., H. Glicken, R. J. Janda, and P. M. Douglass (1981), Catastrophic rockslide-avalanche of May 18, in *The 1980 Eruptions of Mount St. Helens, Washington*, edited by P. W. Lipman and D. R. Mullineaux, pp. 347–377, U.S. Geol. Surv., Washington, D. C.
Voight, B., R. J. Janda, H. Glicken, and P. M. Douglass (1983), Nature and mechanics of the Mount St. Helens rockslide-avalanche of 18 May 1980, *Geotechnique*, *33*, 243–273, doi:10.1680/geot.1983.33.3.243.
Walder, J. S., P. Watts, O. E. Sorensen, and K. Janssen (2003), Tsunamis generated by subaerial mass flows, *J. Geophys. Res.*, *108*(B5), 2236, doi:10.1029/2001JB000707.
Ward, S. N. (2001), Landslide tsunami, *J. Geophys. Res.*, *106*(B6), 11,201–11,215, doi:10.1029/2000JB900450.
Ward, S. N., and S. Day (2003), Ritter island volcano—Lateral collapse and the tsunami of 1888, *Geophys. J. Int.*, *154*, 891–902, doi:10.1046/j.1365-246X.2003.02016.x.
Watts, P. (1997), Water waves generated by underwater landslides, PhD thesis, Calif. Inst. of Technol., Pasadena.
Watts, P. (1998), Wavemaker curves for tsunamis generated by underwater landslides, *J. Waterw. Port Coastal Ocean Eng.*, *124*(3), 127–137, doi:10.1061/(ASCE)0733-950X(1998)124:3(127).
Watts, P. (2000), Tsunami features of solid block underwater landslides, *J. Waterw. Port Coastal Ocean Eng.*, *126*(3), 144–152, doi:10.1061/(ASCE)0733-950X(2000)126:3(144).
Weiss, R., H. M. Fritz, and K. Wuennemann (2009), Hybrid modeling of the mega-tsunami runup in Lituya Bay after half a century, *Geophys. Res. Lett.*, *36*, L09602, doi:10.1029/2009GL037814.
Wiegel, R. L. (1955), Laboratory studies of gravity waves generated by the movement of a submerged body, *Eos Trans. AGU*, *36*(5), 759–774.
Wiegel, R. L., E. K. Noda, E. M. Kuba, D. M. Gee, and G. F. Tornberg (1970), Water waves generated by landslides in reservoirs, *J. Waterw. Harbors Coastal Eng. Div.*, *96*(2), 307–333.
Williams, J. M. (1985), *Tables of Progressive Gravity Waves*, Pitman, Boston, Mass.
Zweifel, A., and W. H. Hager (2006), Plane impulse waves in reservoirs, *J. Waterw. Port Coastal Ocean Eng.*, *132*(5), 358–368, doi:10.1061/(ASCE)0733-950X(2006)132:5(358).